Magnetic Field and Symmetry Effects in Small Quantum Dots[¶]

R. G. Nazmitdinov

Bogoliubov Laboratory of Theoretical Physics Joint, Institute for Nuclear Research, 141980 Dubna, Russia
Departament de Fisica, Universitat de les Illes Balears E-07122 Palma de Mallorca, Spain

Abstract—Shell phenomena in small quantum dots with a few electrons under a perpendicular magnetic field are discussed within a simple model. It is shown that various kinds of shell structures, which occur at specific values for the magnetic field lead to a disappearance of the orbital magnetization for particular magic numbers for noninteracting electrons in small quantum dots. Including the Coulomb interaction between two electrons, we found that the magnetic field gives rise to dynamical symmetries of a three-dimensional axially symmetric two-electron quantum dot with a parabolic confinement. These symmetries manifest themselves as near-degeneracy in the quantum spectrum at specific values of the magnetic field and are robust at any strength of the electron-electron interaction. A remarkable agreement between experimental data and calculations exhibits the important role of the thickness for the two-electron quantum dot for analysis of ground state transitions in a perpendicular magnetic field.

1. INTRODUCTION

The development of semiconductor technology has made it possible for the confinement of a finite number of electrons in a localized three-dimensional space of a few hundreds Angstroms [1, 2]. This mesoscopic system, which was made up of artificially trapped electrons between a few layers of various semiconductors and called quantum dot (QD), opens new avenues in the study of the interplay between quantum and classical behavior at a low–dimensional scale. The quantum dot is formed by removing the electrons outside the dot region with external gates (lateral dot), or by etching out the material outside the dot region (vertical dot) (see, for example, [3–5]). The dot is connected to its environment by electrostatic barriers, the so called source and drain contacts, and gates to which one can apply a voltage V_g. In order to observe quantum effects, QDs are cooled down to well below 1 K. Note that in vertical QDs there is a strong screening of the Coulomb interactions in contrast to lateral ones (see [4]). It results in strong quantum effects for the confinement potential on dynamics of confined electrons. The main effects discussed in the present review are directly relevant to vertical dots.

The smaller the quantum dot is, the larger the prevalence of quantum effects is upon the static and dynamic properties of the system. Almost all parameters of QDs: size, strength of a confining potential, number of electrons, coupling between dots, dielectric environment, the shape of tunneling barriers, as well as external parameters, such as temperature and magnetic, electrical and/or electro-magnetic fields,—can be varied in a controlled way. It is precisely to stress this controllability that the names *artificial atoms* and *quantum dots* have been coined. Therefore, QDs can be considered as a tiny laboratory allowing the direct investigation of fundamental properties of charge and spin correlations at the atomic scale [3, 4, 6, 7]. Another strong motivation for studying the properties of QDs is due to a rapid development in the field of quantum computing, since the entangled states of the electrons confined in a quantum dot may give a natural realization of a quantum bit or "qubit" [5]. It is expected that QDs could lead to novel device applications in fields such as quantum cryptography, quantum computing, optics and optoelectronics, information storage, biology (fluorescent labeling of cellular targets).

The simplest approach to a description for finite quantum systems of interacting Fermions is based on the idea that the interactions create an effective potential in which particles are assumed to move independently. For finite Fermi system like nuclei and metallic clusters, the bunching of single-particle levels known as shells [8–10] is one consequence of this description, since the mean free path is comparable with the size of the system. A remarkable stability is found in nuclei and metallic clusters at magic numbers that correspond to closed shells in the effective potential.

For small quantum dots, where the number of electrons is well defined ($N \leq 30$), the mean free path of the electrons at Fermi energy ($\lambda_F \sim 100$ nm) appears to be larger or comparable with the diameter of the dot ($d \sim$

[¶] The text was submitted by the author in English.

10–100 nm) [11]. Therefore, it seems natural to assume that the properties of the electron states in QDs close to the Fermi level should be determined by the effective mean field of the "artificial atom," produced by a non-trivial interplay of the external confinement governed by gate voltage and electron-electron interaction. However, the atom–quantum dot analogy should not be carried too far: unlike electrons in an isolated atom, carriers in semiconductor QDs interact strongly with lattice vibrations and could be strongly influenced by defect, surface, or interface states. In contrast to real atoms, for which the confining Coulomb potential is well known, the forces that keep the carriers in place in self-organized traps are difficult to estimate from first principles. The exact shape and composition of the traps are often not well known and depend on the growth procedure; in addition, complications are introduced by the complex band structure of the strained material and, in some cases, the effect of piezoelectric forces. A good assessment of an effective confining potential inside the dot can be obtained from a combined study of the ground-state and excitation energies. Ground-state energies are investigated by capacitance spectroscopy or by single electron tunnelling spectroscopy [4]. Far-infrared spectroscopy is used to study the excitations of N-electron states in the dots (see below).

The electron states of few-electron quantum dots subjected to a strong magnetic field have been studied extensively in various experiments. The electrodynamic response (far-infrared spectroscopy) of QDs is expected to be dominated by the many-body effects produced by confined and interacting electrons. Sikorski and Merkt [12] found experimentally, however, the surprising result that the resonance frequencies in the magneto-optical spectrum are independent of the number of electrons in the QD. In these systems which are experimentally realized the extension in the $x - y$-plane is much larger than in the z-direction. Based on the assumption that the extension in the z-direction can be effectively considered zero, a good description of the far-infrared resonance frequencies has been found [12] within a two-dimensional (2D) harmonic oscillator model in the presence of a magnetic field [13]. This result was interpreted as a consequence of Kohn's theorem [14], which is applied for a parabolic potential [15, 16]. According to this theorem, for the parabolic confinement the total Hamiltonian can be divided into two parts, the center-of-mass motion and the relative motion, which contains the electron-electron interaction. The wavelength of the external laser field far exceeds the average dot diameter and, therefore, can be approximated by a dipole electric term only. Since the radiation of an external electric dipole field couples only to the center-of-mass motion and does not affect the relative motion, the dipole resonance frequencies should be exactly the same as those of the non-interacting system with the parabolic confinement and, therefore, be independent on the electron-electron interaction. The more complicated resonance structure

observed in [17, 18] raised, however, the question as to the validity of Kohn's theorem for QDs. In order to describe the experimental data it was assumed that there is a deviation of the confining potential from the parabolic form, and different phenomenological corrections have been introduced [19, 20]. Considering the external gates and the surrounding of a two-electron QD as the image charge, it was shown in [21] that the effective potential has, indeed, anharmonic corrections to the parabolic potential. However, their contribution becomes less important with the increase of the magnetic field strength.

Recent single-electron capacitance spectroscopy experiments in vertical QDs [22–24] provide further strong evidence in favor of the parabolic potential as an effective confinement potential in small QDs. In these experiments shell structure phenomena have been observed clearly. In particular, the energy needed to place the extra electron (addition energy) into a vertical QD at zero magnetic field has characteristic maxima that correspond to the sequence of the magic numbers of a 2D harmonic oscillator. The energy gap between filled shells is approximately $\hbar\omega_0$, where $\hbar\omega_0$ is the lateral confinement energy of the 2D harmonic oscillator. In fact, these atomic-like features when the confining energy is comparable to, or larger than the interaction energy have been predicted before in a few publications [25–27]. Indeed, for a small dot size and small number of electrons the confinement energy becomes prevalent over the Coulomb energy. This has been confirmed for two interacting electrons in an external parabolic potential [28] and by calculations of the effective single-particle levels within the density-functional theory for electron numbers $N \sim 100$ [29] (see for a recent review [30]).

These experimental and theoretical studies lead to the conclusion that, indeed, for a few-electron small QDs the parabolic potential is a good approximation for the effective confinement. It is worthwhile to say that for the typical voltage ~1 V applied to the gates, the confining potential in small quantum dots is some eV deep which is large compared to the few meV of the confining frequency. Hence, the electron wave function is localized close to the minimum of the well, which always can be approximated by a parabolic potential.

Depending on the experimental setup the spectrum of a quantum dot display's shell structure or follows the prediction of random matrix theory (see for a review [31]). In this short survey we will discuss some results related to a manifestation of symmetries in small QDs. The rearrangement of the intrinsic structure of small QDs under the perpendicular magnetic field can be traced within a simple model introduced for the first time in [26]. Using this model we will consider in Section 2 the evolution of shell effects upon the perpendicular magnetic field. In spite of simplicity the model contains some basic features of the structural properties of small QDs. For instance, the model describes the

effect of spontaneous breaking of the symmetry of the mean field due to the magnetic field and number of electrons. Probably, due to the above reasons the model has been "*rediscovered*" by other authors (see, e.g., [30]). In Section 3 we will trace the dynamical effects of the confinement strength, the magnetic strength, the Coulomb repulsion, and their mutual interplay in the model for a two-electron QD. We will show that at a particular strength of the magnetic field the nonlinear dynamics of two-electron QD becomes separable. Section 4 will be devoted to a comparison of theoretical and experimental results for the ground state energies of two-electron quantum dots in a perpendicular magnetic field. In Section 5 we will discuss the concept of the effective charge, which allows inlcusion of the effect of the dot thickness for the analysis of the ground state transitions in 2D approximation. The conclusions are finally drawn in Section 6. Two Appendices provide some details of calculations.

2. SHELL EFFECTS IN SMALL QUANTUM DOTS

To analyze experimental data a few approximations are commonly used. The underlying lattice of the semiconductor material is taken into account by using the effective mass for the conduction electrons, and a static dielectric constant, reducing the Coulomb repulsion. As it was mentioned in the Introduction, an effective trapping potential in small QDs with a few electrons is approximated by a parabolic confinement quite well. The ground state energy of the dot is calculated with the aid of the total energy of the closed dot. This approximation is well justified, when the tunneling between QD and the source and drain is relatively weak. Using these approximations one can study the effect of the magnetic field on the electron spectrum of the dot. Hereafter, the magnetic field acts perpendicular to the plane (xy) of motion of electrons.

Thus, the Hamiltonian of an isolated quantum dot with N electrons in a perpendicular magnetic field reads

$$H = H_0 + H_{int}$$

$$= \sum_{j=1}^{N} \left[\frac{1}{2m^*} \left(\mathbf{p}_j - \frac{e}{c} \mathbf{A}_j \right)^2 + U(\mathbf{r}_j) + \mu^* \sigma_z(j) B \right]$$

$$+ \sum_{i>j=1}^{N} \frac{k}{|\mathbf{r}_i - \mathbf{r}_j|}, \quad (1)$$

where $k = e^2/4\pi\varepsilon_0\varepsilon_r$. Here, e, m^*, ε_0, and ε_r are the unit charge, effective electron mass, vacuum and relative dielectric constants of a semiconductor, respectively. The confining potential is approximated by a three-dimensional harmonic oscillator potential (HO) $U(\mathbf{r}) = m^*[\omega_x^2 x^2 + \omega_y^2 y^2 + \omega_z^2 z^2]/2$, where $\hbar\omega_i$ ($i = x, y, z$) are the energy scales of confinement in the x, y, z directions, respectively. The effective spin magnetic moment is

$\mu^* = g_L\mu_B$ with $\mu_B = |e|\hbar/2m_e c$ and σ_z is the Pauli matrix.

2.1. Shell Structure in Simple Models

To illuminate shell phenomena in QDs let us start with a simple model [26, 32, 33]. The effect of an external homogeneous magnetic field can be calculated exactly for a three-dimensional (3D) harmonic oscillator potential irrespective of the direction of the field [26, 32]. For the perpendicular magnetic field we choose the vector potential with a gauge $\mathbf{A} = \frac{1}{2} \mathbf{B} \times \mathbf{r} = \frac{1}{2} B(-y, x, 0)$. In this case the electronic spectrum generated by the Hamiltonian (1) without interaction is determined by a sum $H_0 = \sum_i^N h_i$ of a single-particle harmonic oscillator Hamiltonians $h = h_0 + h_z$ where

$$h_0 = \frac{p_x^2 + p_y^2}{2m^*} + \frac{m^*}{2} \sum_{i=1}^{2} \omega_i^2 x_i^2 - \omega_L l_z. \quad (2)$$

Here, for a perpendicular magnetic field we have

$$\omega_1^2 = \omega_x^2 + \omega_L^2, \quad \omega_2^2 = \omega_y^2 + \omega_L^2, \quad (3)$$

and $\omega_L = |e|B/(2m^*c)$. Since the orbital momentum l_z

$$l_z = xp_y - yp_x \quad (4)$$

couples lateral variables, the dynamics in z direction is determined by one-dimensional harmonic oscillator $h_z = p_z^2/2m^* + m^*\omega_z^2 z^2/2$.

Before we proceed a few remarks are in order. It is true that the external field is the dominant part of the mean field, and thus the effective confining potential should reflect the main features of it. Yet it must also contain the effect of the interplay between Coulomb forces and the external fields that are governed by the charges in the adjacent layers and gates and the magnetic field. Due to these considerations, we assume that the confining potential should also take into account the changes that affect the properties of the single-electron states owing to a variation of the homogeneous magnetic field as well as the slab thickness. We assume that the system adjusts itself under the influence of the magnetic field and a particle number. Minimizing E_{tot} associated with the Hamiltonian given by Eq. (1) (without the interaction term), a variation of the magnetic field strength leads to a corresponding change of the effective confining potential which is given by the oscillator frequencies. In other words, for a given magnetic field, we must seek the minimum of E_{tot} under variation of the oscillator frequencies. In this way, we accommodate the effect of the interplay between Coulomb forces and external fields such as the external confinement and the magnetic field. Here, the Pauli principle is essential as it limits the accessible quantum configuration space for
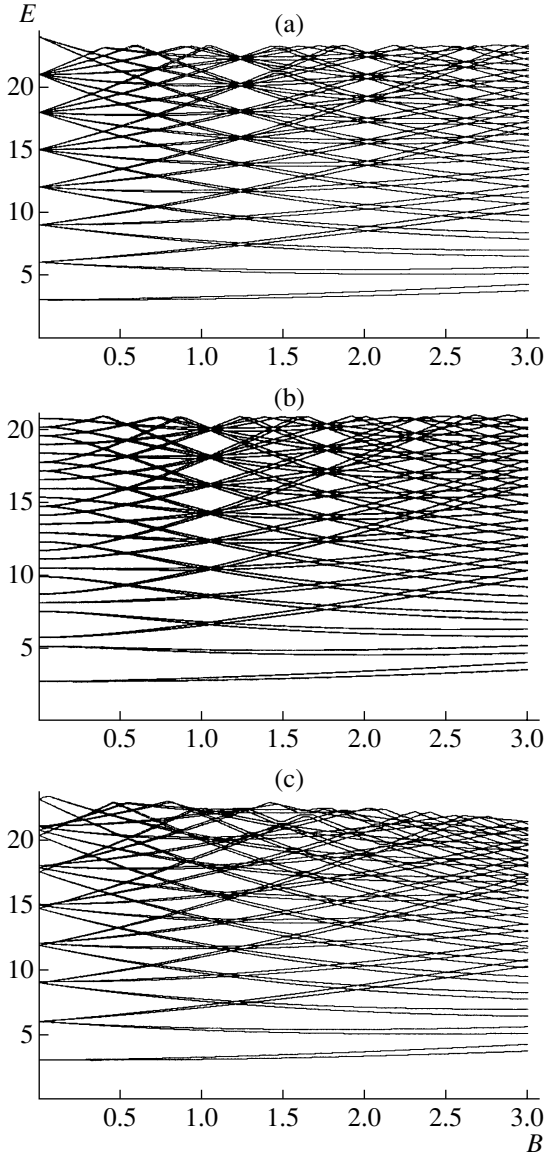
Fig. 1. Single-particle spectra as a function of the magnetic field strength. Spectra are displayed for (a) a plain isotropic ($\omega_x = \omega_y$) two-dimensional oscillator, (b) a deformed and (c) an isotropic oscillator including an L^2-term. For better illustration the value $2\mu^*$ is used for the spin magnetic splitting in all figures. From [33].

$$\frac{d}{d\omega_k}\langle g|H_0|g\rangle = \left\langle g\left|\frac{dH_0}{d\omega_k}\right|g\right\rangle \qquad (6)$$

the useful condition

$$\omega_x^2\langle g|x^2|g\rangle = \omega_y^2\langle g|y^2|g\rangle = \omega_z^2\langle g|z^2|g\rangle, \qquad (7)$$

which must be obeyed at the minimum of E_{tot}. We restrict ourselves to consideration of a thin slab which extends essentially in two dimensions. This is achieved by varying only ω_x and ω_y in the minimization procedure while keeping ω_z fixed at a value which is, say, a few times larger than the other two frequencies. In this case only $\omega_x^2\langle g|x^2|g\rangle = \omega_y^2\langle g|y^2|g\rangle$ can be fulfilled. Choosing different (fixed) values of ω_z allows for the study of the dependence of the results on the slab thickness.

Since the electron interaction is crucial only for partially filled electronic shells (see, for example, [4, 30]) we deal in this section mainly with closed shells. This case corresponds to the quantum limit $\hbar\omega_0 > k/l_0$, where k/l_0 is the typical Coulomb energy and $l_0 = (\hbar/m^*\omega_0)^{1/2}$ is the effective oscillator length. In fact, for small dots, where large gaps between closed shells occur (see results of calculations in [25, 27, 29]), the electron interaction plays the role of a weak perturbation, which can be neglected. But even in the regime $\hbar\omega_0 < k/l_0$ a distinctively larger addition energy is needed, if an electron is added to a closed shell. We do not take into account the effect of finite temperature; this is appropriate for experiments which are performed at temperatures $k_B T \ll \hbar\omega_0$ with $\hbar\omega_0$ being the mean level spacing. In the following we use meV for the energy and T (Tesla) for the magnetic field strength. The effective mass is chosen as $m^* = 0.067 m_e$ for GaAs, which yields, for $N \approx 15$, the size $R \approx 320$ Å and $\hbar\omega_0 = 3$ meV [32]. The effective mass determines the orbital magnetic moment μ_B^{eff} for electrons through the relation $\hbar\omega_L = \mu_B B m_e/m^* = \mu_B^{\text{eff}} B$ and leads to $\mu_B^{\text{eff}} \approx 15\mu_B$. The magnetic orbital effect is much more enhanced in comparison with the magnetic spin effect (with the effective Lande factor $|g_L| = 0.44$), yet the tiny spin splitting does produce signatures as we see below.

Since we consider the dot with a fixed ω_z ($z \sim 0$), shell effects are determined by the ratio of the eigenmodes $\Omega_\pm$ in the lateral plane (see for details Appendix A and [32]). Shell structure occurs whenever the ratio of the two eigenmodes $\Omega_\pm$ of the Hamiltonian H_0 is a rational number with a small numerator and denominator. Closed shells are particularly pronounced if the ratio is equal to one (for $B = 0$) or two (for $B \approx 1.23$) or three (for $B \approx 2.01$) and lesser pronounced if the ratio is 3/2 (for $B = 0.72$) or 5/2 (for $B = 1.65$) for a circular case $\omega_x = \omega_y$ (see Fig. 1a). Note that, for better illustration, we used for the spin splitting the value $2\mu_B$ instead of the correct μ^* in all Figures; the discussions and con-

the electrons. The variation cannot be unrestricted as the confining potential encloses a fixed number of electrons, and assuming that the electron density area does not change, we are led to a fixed volume constraint which translates into the subsidiary condition $\omega_x\omega_y\omega_z = \omega_0^3$ with ω_0 fixed. Denoting the Lagrange multiplier by λ we solve the variational problem

$$\delta(\langle g|H_0|g\rangle - \lambda\omega_x\omega_y\omega_z) = 0, \qquad (5)$$

where $|g\rangle$ denotes the ground state. From Eq. (5) we obtain, after differentiation with respect to the frequencies and using Feynman's theorem [34]

clusions are based on the correct value. The values given here for B depend on m^* and $\omega_{x,y}$. As a consequence, a material with an even smaller effective mass m^* would show these effects for a correspondingly smaller magnetic field. For $B = 0$ the magic numbers (including spin) turn out to to be the usual sequence of the two-dimensional isotropic oscillator, that is 2, 6, 12, 20, ... For $B \approx 1.23$ we find a new shell structure as if the confining potential would be a deformed harmonic oscillator without a magnetic field. The magic numbers are 2, 4, 8, 12, 18, 24, ... which are just the numbers obtained from the two-dimensional oscillator with $\omega_> = 2\omega_<$ ($\omega_>$ and $\omega_<$ denote the larger and smaller value of the two frequencies). Similarly, we get for $B \approx 2.01$ the magic numbers 2, 4, 6, 10, 14, 18, 24, ... which corresponds to $\omega_> = 3\omega_<$. If we start from the outset with a deformed mean field $\omega_x = (1 - \beta)\omega_y$ with $\beta > 0$, the degeneracies (shell structure) lifted at $B = 0$ re-occur at higher values for B. In Fig. 1b we display an example referring to $\beta = 0.2$. The significance of this finding lies in the restoration of the shell structures by the magnetic field in an isolated QD that does not give rise to magic numbers at a zero field strength due to deformation. We mention that the choice $\beta = 0.5$ would shift the pattern found at $B \approx 1.23$ in Fig. 1a to the value $B = 0$. Closed shells are obtained for values of B and β which yield $\Omega_+/\Omega_- = l = 1, 2, 3, \dots$.

Indeed, it is the shell structure caused by the effective mean field that produces the maxima that are observed experimentally in the addition energy

$$\Delta\mu = \mu(N) - \mu(N-1) \qquad (8)$$

for $N = 2, 6, 12$ electrons (see [22]), where $\mu(N)$ is an electrochemical potential of an N-electron dot. In order to shed light on this phenomenon let us calculate $\Delta\mu$ in a constant-interaction (CI) model that provides an approximate description of the electronic states of QDs (see for details [4]). In the CI model the total ground state energy of an N-electron dot is

$$E(N) = [e(N - N_0) - C_g V_g]^2 / 2C + \sum_i^N \varepsilon_i, \qquad (9)$$

where $N = N_0$ for gate voltage $V_g = 0$. The term $C_g V_g$ represents the charge (a continuous variable) induced on the dot by gate voltage V_g, through the gate capacitance, C_g. It is assumed that the Coulomb interactions of an electron on the dot with all other electrons, in and outside the dot, are parameterized by a constant total capacitance C. The total capacitance between the dot and the source, drain and gate is $C = C_s + C_d + C_g$. The quantum contribution is determined by the sum over all occupied single-particle energies ε_i, which depend on the magnetic field. In the CI model it is assumed that the single-particle spectrum is calculated for noninteracting electrons. The electrochemical potential of the dot is defined as $\mu_{dot} = E(N) - E(N-1)$. Electrons can flow from the source (left) to the drain (right) through a

transport (bias) window eV_{sd} when $\mu_{left} > \mu_{dot}(N) > \mu_{right}$ (with $-|e|V_{sd} = \mu_{left} - \mu_{right}$). With the aid of Eq. (9) one obtains the additional energy

$$\Delta\mu = \varepsilon_N - \varepsilon_{N-1} + e^2/C, \qquad (10)$$

where ε_N is the highest filled single-particle state for an N-electron dot, e^2/C is the classical electrostatic energy. In the CI model additions of single electrons are periodic in e^2/C, since the difference $\varepsilon_N - \varepsilon_{N-1}$ is usually neglected. In reality, however, it is the fluctuations (shell effects) of the difference that matters, at least for small QDs. A similar effect is known in nuclear physics and for metallic clusters. There, shell effects due to single-particle motion create minima in the total potential energy surface, which is dominated by the bulk energy, which is the classical liquid drop energy [9, 10]. The analogy goes further in that, in an isolated small QD, the external magnetic field acts like the rotation on a nucleus thus creating a new shell structure; in this way, superdeformation (axis ratio 2 : 1) has been established for rotating nuclei owing to the shell gaps in the single-particle spectrum [9].

In [32] we have obtained various shapes of the QD by energy minimization. In this context it is worth noting that at the particular values of the magnetic field, where a pronounced shell structure occurs, the energy minimum would be obtained for circular dots, if the particle number were chosen to be equal to the magic numbers. Deviations from those magic numbers usually give rise to deformed shapes at the energy minimum. To what extent these "spontaneous" deformations actually occur (which is the Jahn–Teller effect [35]), is subject to more detailed experimental information. The far-infrared spectroscopy in a small isolated QD could be a useful tool to provide pertinent data [32].

The question arises as to what extent our findings depend upon the particular choice of the mean field. Here we confirm the qualitative argument presented above that for sufficiently low electron numbers virtually any binding potential would produce the patterns found for the harmonic oscillator. The Coulomb interaction lowers the electron levels for increasing magnetic quantum number $|m|$ (see, e.g., [28]). We add to the Hamiltonian H_0 (see Eq. (1)) the term $-\gamma\hbar\omega_L L^2$, where L is the dimensionless z-component of the angular momentum operator. For $\gamma > 0$ the additional term lowers the energy levels of higher angular momenta and mimics the Coulomb interaction effect. As a consequence, it has the effect of interpolating between the oscillator and the square well single-particle spectrum. For $\omega_x \neq \omega_y$ and $\gamma \neq 0$ the combined Hamiltonian $H' = H_0 - \gamma\hbar\omega_L L^2$ is nonintegrable [36] and the level crossings encountered in Fig. 1 become avoided level crossings. The essential effect upon the lower end of the spectrum can be seen in the isotropic oscillator where the magnetic quantum number m is a good quantum number. In this case $H' = H_0^{isotr} - \gamma\hbar\omega_L m^2$. In Fig. 1c we
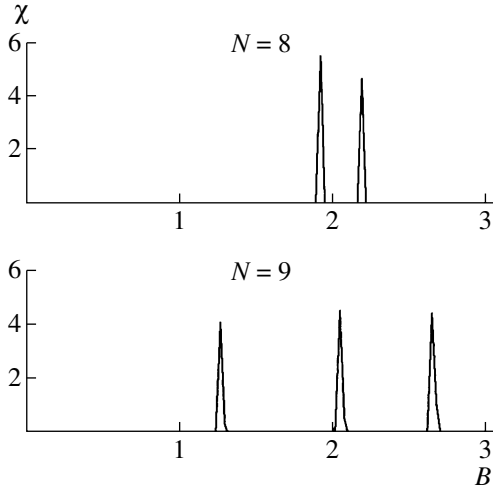
Fig. 2. Magnetic susceptibility $\chi = -\partial^2 E_{tot}/\partial B^2$ in arbitrary units as a function of the magnetic field strength for the isotropic oscillator without L^2-term. E_{tot} is the sum of the single-particle energies filled from the bottom up to the electron number N. From [33].
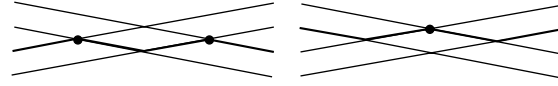

Fig. 3. Blow ups of the relevant level crossings explaining the features in Fig. 2. The left and right hand refers to $N = 8$ and 9, respectively. From [33].

display a spectrum of such H'. The shell structure, which prevails for $\gamma = 0$ throughout the spectrum at $B \approx 1.23$ or $B \approx 2.01$, is now disturbed to an increasing extent with an increasing shell number. However, for the parameters chosen the structure is still clearly discernible for about seven shells, which is for particle numbers up to about 25. The lifting of the degeneracies at $B = 0$ is also clearly seen where the levels are split according to the absolute values of $|m|$; it is this splitting which gives us guidance in choosing an appropriate value for γ. For $B = 0$ single particle levels lie between the corresponding degenerate levels pertaining to the HO and the two-dimensional square well where the splitting of these levels is very strong.

2.2. Magnetic Properties

When the magnetic field is changed continuously for a QD of a fixed electron number, the ground state will undergo a rearrangement at the values of B, where level crossings occur [28]. In fact, it leads to a strong variation in the magnetization [6] and should be observable also in the magnetic susceptibility $\chi = -\partial E_{tot}^2/\partial B^2$ as it is proportional to the second derivative of the total energy with respect to the field strength. While details may be modified by electron correlations, we think that the general features discussed below should be preserved.

In Fig. 2 we clearly discern distinct patterns depending on the electron number, in fact, the susceptibility appears to be a fingerprint pertaining to the electron number. All features of Fig. 2 can be understood from the single-particle spectra displayed in Fig. 1. If there is no level crossing, the second derivative of E_{tot} is a

smooth function. The crossing of two occupied levels does not change the smoothness. In contrast, if an unoccupied level crosses the last occupied level, the second derivative of E_{tot} must show a spike. In this way, we understand the *even-odd effect* when comparing $N = 8$ with $N = 9$ in Fig. 2. The spin splitting caused by the magnetic field at $B \approx 2.01$ for $N = 8$ is absent for $N = 9$. This becomes evident when looking at a blow up of this particular level crossing which is illustrated in Fig. 3, where the last occupied level is indicated as a thick line and the points where a spike occurs are indicated by a dot. Note that the splitting is proportional to the effective spin magnetic moment μ^*.

Spikes of the susceptibility are associated with a spin flip for even electron numbers. They are brought about by the crossing of the top (bottom) with the bottom (top) line of a double line. Hence, both lines of the double splitting in Fig. 3 yield a spin flip ($N = 8$), but neither of the single lines ($N = 9$). Strictly speaking, the spikes are δ-functions with a factor, which is determined by the angle at which the two relevant lines cross. Our figures are numerical results that do not exactly reflect this feature. If the level crossings were replaced by avoided crossings (Landau–Zener crossings), the lines would be broadened. This would be the case in the present model for $\gamma > 0$ and $\beta > 0$. Finite temperature will also result in line broadening. We would like to point out that the *even-odd effect*, discussed for the first time in [33], has been later observed by Tarucha and Austing [37].

We now focus on the special cases which give rise to a pronounced shell structure, which is when the ratio $\Omega_+/\Omega_- = l = 1, 2, 3, \ldots$. To avoid elaborate expressions we analyze in detail the circular shape ($\omega_x = \omega_y = \omega_0$, $\langle z^2 \rangle = 0$) for which the eigenmodes, Eq. (A.5), become $\Omega_\pm = (\Omega \pm \omega_L)$ with $\Omega = \sqrt{\omega_0^2 + \omega_L^2}$ [13]. In this case the total energy for the closed QD is (see Appendix A)

$$E_{tot} = \Omega_+ \Sigma_+ + \Omega_- \Sigma_- - \mu^* B \langle S_z \rangle \qquad (11)$$

with $\Sigma_\pm = \Sigma_j^N (n_\pm + 1/2)_j$ and shell number $N_{sh} = n_+ + n_-$ [32]. We find for the magnetization $M = -dE_{tot}/dB$, taking into account after differentiation of the total energy (11) that $\Omega_+ = l\Omega_-$,

$$M = \mu_B^{eff} \left(1 - \frac{\omega_L}{\Omega}\right)(\Sigma_- - l\Sigma_+) - \mu^* \langle S_z \rangle. \qquad (12)$$

For a completely filled shell $\langle S_z \rangle = 0$, since, for the magnetic field strengths considered here, the spin orientations cancel each other (see Fig. 1). From the orbital motion we obtain for the susceptibility

$$\chi = -d^2 E_{\text{tot}}/dB^2 = -\frac{\mu_B^{\text{eff}^2}}{\hbar\Omega}\left(\frac{\omega_0}{\Omega}\right)^2 (\Sigma_+ + \Sigma_-). \quad (13)$$

It follows from Eq. (13) that, for a completely filled shell, the magnetization owing to the orbital motion leads to diamagnetic behavior. For a zero magnetic field ($l = 1$) the system is paramagnetic and the magnetization vanishes ($\Sigma_- = \Sigma_+$). The value $l = 2$ is attained at $B \approx$ 1.23. When calculating Σ_- and Σ_+ we have to distinguish between the cases, where the shell number N_{sh} of the last filled shell is even or odd. With all shells filled from the bottom we find (i) for the last filled shell number even:

$$\Sigma_+ = \frac{1}{12}(N_{\text{sh}} + 2)[(N_{\text{sh}} + 2)^2 + 2] \quad (14)$$

and

$$\Sigma_- = \frac{1}{6}(N_{\text{sh}} + 1)(N_{\text{sh}} + 2)(N_{\text{sh}} + 3), \quad (15)$$

which implies

$$M = -\mu_B^{\text{eff}}(1 - \omega_L/\Omega)(N_{\text{sh}} + 2)/2 \quad (16)$$

and (ii) for the last filled shell number odd:

$$\Sigma_+ = \frac{1}{2}\Sigma_- = \frac{1}{12}(N_{\text{sh}} + 1)(N_{\text{sh}} + 2)(N_{\text{sh}} + 3), \quad (17)$$

which, in turn, implies $M = 0$.

Therefore, if $\Omega_+/\Omega_- = 2$, the orbital magnetization vanishes for the magic numbers 4, 12, 24, … while it leads to diamagnetism for the magic numbers 2, 8, 18, …. A similar picture is obtained for $\Omega_+/\Omega_- = 3$, which happens at $B \approx 2.01$: for each third filled shell number (magic numbers 6, 18, …) the magnetization is zero. Since the results presented are due to shell effects, they do not depend on the assumption $\omega_x/\omega_y = 1$, which was made to facilitate the discussion. The crucial point is the relation $\Omega_+/\Omega_- = l = 1, 2, 3, …$ which can be obtained for a variety of combinations of the magnetic field strength and the ratio ω_x/ω_y as is illustrated in Fig. 1 (see also Fig. 2 in [33]). Whenever the appropriate combination of field strength and deformation is chosen to yield, say, $l = 2$, our findings apply.

Concluding this section we note that consideration of the third dimension may improve the agreement with experimental data. In fact, magic numbers observed at zero magnetic field [22] can be reproduced as well by the 3D harmonic oscillator model with additional *axial octupole and hexadecopole* deformations [38]. In the superdeformed HO a certain combination of strengths for these two terms leads to the shell structure of the 2D harmonic oscillator model. We will consider below a realistic model of two interacting electrons in a 3D quantum dot with a parabolic confinement [39, 40].

3. HIDDEN SYMMETRIES IN A TWO-ELECTRON QUANTUM DOT

A three-dimensional harmonic oscillator with frequencies in rational ratios (RHO) and a Coulomb system are benchmarks for the hidden symmetries, which account for the accidental degeneracies of their quantum spectra (see, e.g., [41]). Recent advances in nanotechnology create a remarkable opportunity to trace their dynamical interplay in QDs. Indeed, competition between a confining potential, approximated well by the HO, and the repulsive electron-electron interaction produces a rich variety of phenomena, for example, in a two-electron QD under a perpendicular magnetic field (see [4, 7] and references therein). In fact, a two-electron QD becomes a testing–ground for different quantum-mechanical approaches [7] and experimental techniques that could provide highly accurate data for this system [2, 4].

If the HO and the Coulomb potential are combined, most of the symmetries are expected to be broken. Nevertheless, in particular cases, the Coulomb (Kepler) system and the RHO may have common symmetries, as it was already noticed a long time ago [42]. The authors of [42] could not find, however, a physical application for this phenomenon. These symmetries were rediscovered in the analysis of laser–cooled ions in a Paul trap [43] and of the hydrogen atom in the generalized van der Waals potential [44]. The major aspect of this section is to demonstrate that the hidden symmetries could be observed in a two-electron QD with a 3D effective parabolic confinement under a tunable perpendicular magnetic field. Note that these symmetries have been overlooked in plain quantum-mechanical models. Therefore, to this aim we focus our analysis upon the nonlinear classical dynamics of the system. At certain conditions the motion becomes integrable and this indicates the existence of the symmetries in the quantum spectrum.

3.1. The Center-of-Mass and Relative Motion Hamiltonians

The Hamiltonian of a two-electron QD in a magnetic field is determined by Eq. (1). In this section we consider a 3D axially symmetric HO, i.e., with confining frequencies ω_z and $\omega_x = \omega_y = \omega_0$. In contrast to a 2D description of the QD this approximation provides a more accurate description of various experimental features (see next section). In the present analysis we neglect the spin interaction (the Zeeman term), since the corresponding energy is small compared to the confinement and the Coulomb energies and is not important for our discussion.

Introducing the relative and center-of-mass (CM) coordinates $\mathbf{r} = \mathbf{r}_1 - \mathbf{r}_2$, $\mathbf{R} = \frac{1}{2}(\mathbf{r}_1 + \mathbf{r}_2)$ the Hamiltonian (1) can be separated into the CM and relative motion terms [28] due to the Kohn theorem (see also Sections 1, 2)

$$H = H_{cm} + H_{rel}, \qquad (18)$$

where

$$H_{cm} = \frac{\mathbf{P}^2}{2M^*} - \omega_L L_z + \frac{M^*}{2}[\omega_\rho^2(X^2 + Y^2) + \omega_z^2 Z^2], \qquad (19)$$

$$H_{rel} = \frac{\mathbf{p}^2}{2\mu} - \omega_L l_z + \frac{\mu}{2}[\omega_\rho^2(x^2 + y^2) + \omega_z^2 z^2] + \frac{k}{r}. \qquad (20)$$

Here $M^* = 2m^*$ and $\mu = m^*/2$ are the total and reduced masses, ω_L is the Larmor frequency and L_z and l_z are the z-projections of the angular momenta for the CM and relative motions, respectively. The effective confinement frequency in the ρ-coordinate $\omega_\rho = (\omega_L^2 + \omega_0^2)^{1/2}$ depends through ω_L on the magnetic field. In this way the magnetic field can be used to control the effective lateral confinement frequency of the QD for a fixed value of the vertical confinement, i.e. the ratio ω_z/ω_ρ.

The CM term is described by the axially symmetric 3D harmonic oscillator (ω_0, ω_0, ω_z) in a magnetic field, which eigenenergies are the sum of Fock–Darwin levels and oscillator levels in z-direction

$$E_{cm} = \hbar\omega_\rho(2N + |M| + 1) + \hbar\omega_z(N_z + 1/2) - \omega_L M. \qquad (21)$$

Here $N = 0, 1, \dots$ is the radial quantum number, $M = 0, \pm 2, \pm 3, \dots$ is the azimuthal one and $N_z = 0, 1, 2, \dots$ is the quantum number for center-of-mass excitations in z-direction.

The Hamiltonian for relative motion, using cylindrical coordinates (ρ, φ, z), reads

$$H_{rel} = \frac{1}{2\mu}\left(p_\rho^2 + \frac{l_z^2}{\rho^2} + p_z^2\right) + \frac{\mu}{2}(\omega_\rho^2\rho^2 + \omega_z^2 z^2) + \frac{k}{\sqrt{\rho^2 + z^2}} - \omega_L l_z. \qquad (22)$$

In the following we concentrate on the dynamics of H_{rel}. For our analysis it is convenient to use cylindrical *scaled* coordinates, $\tilde{\rho} = \rho/l_0$, $\tilde{p}_\rho = p_\rho l_0/\hbar$, $\tilde{z} = z/l_0$, $\tilde{p}_z = p_z l_0/\hbar$, where $l_0 = (\hbar/\mu\omega_0)^{1/2}$ is the characteristic length of the confinement potential with the reduced mass μ. The strength parameter k of the Coulomb repulsion goes over to $\lambda = k/(\hbar\omega_0 l_0)$. Although our consideration is general, for the demonstration we chose the values $\hbar\omega_0 \approx 2.8$ meV and $\omega_z = 2.5\omega_0$ which are close to those obtained in our 3D analysis [39] of the experiment [47] (see Section 4). For the effective mass $m^* =$ $0.067m_e$ and the dielectric constant $\varepsilon = 12$, which are typical for GaAs, the value $\lambda = 1.5$. Hereafter, for the sake of simplicity, we drop the tilde, i.e., for the scaled variables we use the same symbols as before scaling.

In these variables the Hamiltonian for the relative motion takes the form (in units of $\hbar\omega_0$)

$$h \equiv \frac{H_{rel}}{\hbar\omega_0} = \frac{1}{2}\left(p_\rho^2 + \frac{m^2}{\rho^2} + p_z^2 + \tilde{\omega}_\rho^2\rho^2 + \tilde{\omega}_z^2 z^2\right) + \frac{\lambda}{r} - \tilde{\omega}_L m, \qquad (23)$$

where $r = (\rho^2 + z^2)^{1/2}$, $\tilde{\omega} \equiv \omega/\omega_0$, $m = l_z/\hbar$.

3.2. The Classical Dynamics and Quantum Spectra

Due to the axial symmetry of the system the φ-motion is separated from the motion in the (ρ, z)-plane and, beside the energy ($\epsilon \equiv h$), the z-component of angular momentum l_z is an integral of motion. Therefore, the magnetic quantum number m is always a good quantum number. Since the Hamiltonian (23) is invariant under the reflection of the origin, the parity π is a good quantum number too.

The classical trajectories can be obtained by solving (numerically) Hamilton's equations

$$\dot{\rho} = p_\rho, \quad \dot{p}_\rho = \frac{m^2}{\rho^3} - \tilde{\omega}_\rho^2\rho + \lambda\frac{\rho}{r^3},$$

$$\dot{\varphi} = \frac{m}{\rho^2} - \tilde{\omega}_L, \quad \dot{m} = 0, \qquad (24)$$

$$\dot{z} = p_z, \quad \dot{p}_z = -\tilde{\omega}_z^2 z + \lambda\frac{z}{r^3},$$

where $\dot{x} \equiv dx/d\tau$ and $\tau = \omega_0 t$ is the scaled time variable. Although the motion in φ is separated from the motion in the (ρ, z)-plane, the problem is in general, non-integrable, since the Coulomb term couples the ρ and z coordinates.

Examination of the Poincaré sections by varying the parameter ω_z/ω_ρ (see Fig. 4 for examples) in the interval (1/10, 10) with a small step indicates that there are five integrable cases. The trivial cases are $\omega_z/\omega_\rho \longrightarrow 0$ and $\omega_z/\omega_\rho \longrightarrow \infty$, which correspond to 1D vertical and 2D circular QDs, respectively. The nontrivial cases are $\omega_z/\omega_\rho = 1/2, 1, 2$. These results hold for any strength of the Coulomb interaction and agree with the results for the Paul trap [43]. Below we discuss the nontrivial cases only. The typical trajectories in cylindrical coordinates are shown in Figs. 5a, 5c.

The results obtained with the aid of the Poincaré surfaces of sections are invariant under the coordinate transformation. On the other hand, the integrability is a necessary condition for the existence of a coordinate system in which the motion can be separated. In turn,
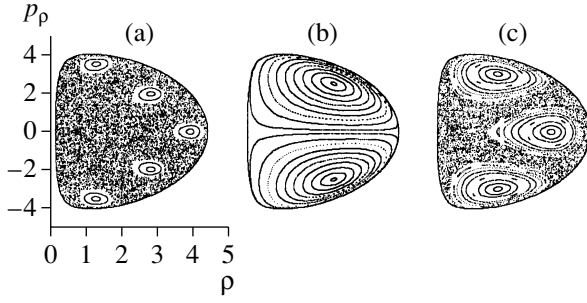
Fig. 4. Poincaré surfaces of sections $z = 0$, $p_z > 0$ of the relative motion ($\lambda = 1.5$, $\epsilon = 10$, $m = 0$) with: (a) $\omega_z/\omega_\rho = 5/2$, (b) $\omega_z/\omega_\rho = 2$, and (c) $\omega_z/\omega_\rho = 3/2$. The section (b) indicates that for the ratio $\omega_z/\omega_\rho = 2$ the system is integrable. From [40].

Fig. 5. Typical trajectories ($\epsilon = 10$, $m = 1$) of the relative motion at $\lambda = 1.5$ for $\omega_z/\omega_\rho = 1$ (a, b) and $\omega_z/\omega_\rho = 2$ (c, d) are shown in cylindrical and prolate spheroidal coordinates, respectively. From [40].

the analogous quantum mechanical system would be characterized by a complete set of quantum numbers.

3.2.1. The case $\omega_\rho = \omega_z$. At the value $\omega'_L = (\omega_z^2 - \omega_0^2)^{1/2}$ the magnetic field gives rise to the spherical symmetry ($\omega_z/\omega_\rho = 1$) in an axially symmetric QD (with $\omega_z > \omega_0$) [39]. In this case the Hamiltonian (23) is separable in (scaled) spherical coordinates

$$h = \frac{p_r^2}{2} + \frac{(\mathbf{l}/\hbar)^2}{2r^2} + \frac{\tilde{\omega}_z^2 r^2}{2} + \frac{\lambda}{r} - \tilde{\omega}'_L m \qquad (25)$$

and the dynamics is integrable. The additional integral of motion is the square of the total angular momentum $\mathbf{l}^2$.

Due to the separability of the Hamiltonian (25) in spherical coordinates the corresponding eigenfunctions can be written in the form

$$\psi(\mathbf{r}) = \frac{\phi_{lm}(r)}{r} Y_{lm}(\vartheta, \varphi). \qquad (26)$$

The functions $\phi_{lm}(r)$ are solutions of the radial equation

$$\left[-\frac{d^2}{dr^2} + \frac{l(l+1)}{r^2} + \tilde{\omega}_z^2 r^2 \right.$$
$$\left. + \frac{2\lambda}{r} - 2(\tilde{\omega}'_L m + \epsilon) \right] \phi_{lm}(r) = 0, \qquad (27)$$

where l and m are the orbital and magnetic quantum numbers, respectively. Equation (27) can be solved numerically and the eigenenergies can be determined iteratively by varying the energy ϵ until the functions ϕ_{lm} fulfill the boundary conditions: $\phi_{lm} \sim r^{l+1}$, $d\phi^{lm}/dr = (l+1)\phi_{lm}/r$ for $r \longrightarrow 0$ and $\phi_{lm} \longrightarrow 0$ for $r \longrightarrow \infty$. Hence, good quantum numbers for this case are (n_r, l, m), where the radial quantum number $n_r = 0, 1, 2, \ldots$ counts over the radial functions $\phi_{n_r, l, m}(r)$ within each
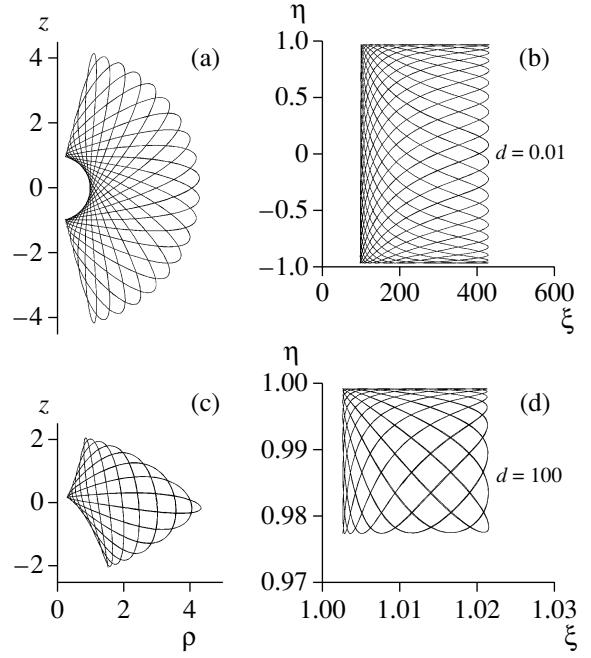
(l, m)-manifold. Moreover, since the potential energy in the Hamiltonian (23) is invariant under the transformation $\mathbf{r} \longrightarrow -\mathbf{r}$, the parity π is also a good quantum number. For the spherical case $\pi = (-1)^l$.

To complete the discussion it should be mentioned that in this case, it is straightforward to use a semiclassical quantization of the Hamiltonian (25) to calculate the spectrum. The procedure reduces to the WKB quantization of r-motion due to the separability of the problem in spherical coordinates. The momentum p_r determined from Eq. (25) enters the action integral

$$I_r = \frac{\hbar}{2\pi} \oint p_r dr = \frac{\hbar}{\pi} \int_{r_{\min}}^{r_{\max}} |p_r| dr, \qquad (28)$$

with the turning points $r_{\min}$, $r_{\max}$ as the positive roots of equation $p_r(r) = 0$. The WKB quantization conditions

$$I_r(\epsilon) = \hbar\left(n_r + \frac{1}{2}\right), \quad n_r = 0, 1, \ldots,$$

$$|\mathbf{l}| = \hbar\left(l + \frac{1}{2}\right), \quad l = 0, 1, \ldots, \qquad (29)$$

$$m = 0, \pm 1, \ldots, \pm l$$

determine the energy levels. For noninteracting electrons ($\lambda = 0$) the analytical calculation of the action integral leads to the (quantum mechanically exact) eigen-energies (A.11). For $\lambda \neq 0$, one can calculate the action integral (28) numerically with a few iterations to

determine the eigenvalues. The results for the spherically symmetric case obtained by the WKB approach and for the cases discussed below can be found in [39].

The restoration of the rotational symmetry of the electronic states by the magnetic field for noninteracting electrons was discussed in Section 2. This phenomenon was also recognized in the results for *interacting* electrons in self-assembled QDs [27]. It was interpreted in [27] as an approximate symmetry that had survived from the noninteracting case due to dominance of the confinement energy over relatively small Coulomb interaction energy. However, as it is clear from the form of Eq. (25), the symmetry is not approximate but *exact* even for strongly interacting electrons because the radial electron-electron repulsion does not break the rotational symmetry.

3.2.2. The case $\omega_z = 2\omega_\rho$ and $\omega_z = \omega_\rho/2$. The spherical coordinates are a particular limit of the spheroidal (elliptic) coordinates well suited for the analysis of the Coulomb systems (see, e.g., [45]). Therefore, to search the separability for the other integrable cases it is convenient to use the spheroidal coordinates (ξ, η, φ), where $\xi = (r_1 + r_2)/d$ and $\eta = (r_1 - r_2)/d$. In the *prolate* spheroidal coordinates $r_1 = [\rho^2 + (z + d)^2]^{1/2}$, $r_2 = r$. The parameter $d \in (0, \infty)$ is the distance between two foci of the coordinate system (with the origin at one of them). In the limit $d \longrightarrow 0$ the motion is separated when $\omega_z/\omega_\rho = 1$ (Fig. 5b). In this limit $\xi \longrightarrow \infty$ such that $r = d\xi/2$ is finite, $\eta = \cos\vartheta$, and we obtain the spherical coordinate system.

Let us turn to the case $\omega_z/\omega_\rho = 2$ which occurs at the value of the magnetic field $\omega_L'' = (\omega_z^2/4 - \omega_0^2)^{1/2}$. In the prolate spheroidal coordinates the motion is separated in the limit $d \longrightarrow \infty$ (Fig. 5d). In fact, at $d \longrightarrow \infty$: $\xi \longrightarrow 1$, $\eta \longrightarrow 1$ such that $\xi_1 = d(\xi - 1)$, $\xi_2 = d(1 - \eta)$ are finite, we obtain the parabolic coordinate system (ξ_1, ξ_2, φ) where $\xi_{1,2} = r \pm z$. In these coordinates the Hamiltonian (23) has the form

$$h = \frac{1}{\xi_1 + \xi_2}\left[2(\xi_1 p_{\xi_1}^2 + \xi_2 p_{\xi_2}^2) + \frac{m^2}{2}\left(\frac{1}{\xi_1} + \frac{1}{\xi_2}\right)\right.$$
$$\left. + \frac{\tilde{\omega}_z^2}{8}(\xi_1^3 + \xi_2^3) + 2\lambda\right] - \tilde{\omega}_L'' m \tag{30}$$

and the equation $(\xi_1 + \xi_2)(h - \epsilon) = 0$ is separated into two decoupled equations for ξ_1 and ξ_2 variables

$$2\xi_j p_{\xi_j}^2 + \frac{m^2}{2\xi_j} + \frac{\tilde{\omega}_z^2}{8}\xi_j^3 - (\epsilon + \tilde{\omega}_L'' m)\xi_j + \lambda = (-1)^j c, \tag{31}$$
$$j = 1, 2.$$

Simple manipulations define the separation constant (see also Appendix B)

$$c = a_z - \tilde{\omega}_\rho^2 \rho^2 z, \tag{32}$$

which is a desired third integral of motion. Here a_z is the z-component of the Runge–Lenz vector $\mathbf{a} = \mathbf{p} \times \mathbf{l} + \lambda\mathbf{r}/(r)$, which is a constant of motion for the pure Coulomb system (i.e., when $\omega_\rho = \omega_z = 0$) [41]. The quantum mechanical counterpart for the integral of motion, Eq. (32), does not commute with the parity operator and we should expect the degeneracy of quantum levels.

Due to the separability of the motion in the parabolic coordinate system, the eigenfunctions of the corresponding Schrödinger equation can be expressed in the form $\psi(\mathbf{r}) = f_1(\xi_1)f_2(\xi_2)e^{im\varphi}$, where the functions f_j are solutions of the equations

$$\frac{d}{d\xi_j}\left(\xi_j\frac{df_j}{d\xi_j}\right) - \frac{1}{4}\left[\frac{m^2}{\xi_j} + \frac{\tilde{\omega}_z^2}{4}\xi_j^3\right.$$
$$\left. - 2(\epsilon + \tilde{\omega}_L'' m)\xi_j + 2\lambda - (-1)^j 2c\right]f_j = 0, \tag{33}$$
$$j = 1, 2.$$

Equation (33) can be solved numerically and the eigenenergies and eigenvalues of c are determined iteratively by varying simultaneously ϵ and c until the functions f_j fulfill the boundary conditions: $f_j \sim \xi_j^{|m|/2}$, $\xi_j df_j/d\xi_j = |m|f_j/2$ for $\xi_j \longrightarrow 0$ and $f_j \longrightarrow 0$ for $\xi_j \longrightarrow \infty$. Let n_1 and n_2 be the nodal quantum numbers of the functions f_1 and f_2, respectively. Note that Eq. (33) is coupled by the constants of motion and, therefore, both functions depend on all three quantum numbers (n_1, n_2, m). The states $|n_1, n_2, m\rangle$ have explicit form (in the coordinate representation)

$$\psi_{n_1, n_2, m}(\mathbf{r}) = f_{n_1}^{(n_2, m)}(\xi_1)f_{n_2}^{(n_1, m)}(\xi_2)\frac{e^{im\varphi}}{\sqrt{2\pi}}. \tag{34}$$

The simple product of these functions does not have a definite parity. Since $\mathbf{r} \longrightarrow -\mathbf{r} \Leftrightarrow \{\xi_1 \longrightarrow \xi_2, \xi_2 \longrightarrow \xi_1, \varphi \longrightarrow \varphi + \pi\}$, the even/odd eigenfunctions are constructed as

$$\psi_{N, k, m}^{(\pm)}(\mathbf{r}) = \frac{e^{im\varphi}}{\sqrt{2}}[f_{n_1}^{(n_2, m)}(\xi_1)f_{n_2}^{(n_1, m)}(\xi_2)$$
$$\pm (-1)^m f_{n_2}^{(n_1, m)}(\xi_1)f_{n_1}^{(n_2, m)}(\xi_2)], \tag{35}$$

where $N = n_1 + n_2$ and $k = |n_1 - n_2|$. These states are the eigenfunctions of h, l_z, $|c|$ and the parity operator. For $|c| > 0$ the eigenstates (35) appear in doublets of different parity and, therefore, of a different total spin. For $c = 0$ in Eqs. (33) $f_1 = f_2$ and, obviously, only the states with parity $\pi = (-1)^m$ exist.

For the magnetic field $\omega_L''' \equiv (4\omega_z^2 - \omega_0^2)^{1/2}$ we obtain the ratio $\omega_z/\omega_\rho = 1/2$. The Hamiltonian (23) expressed in the *oblate* spheroidal coordinates ($r_1 = [z^2 + (\rho + d)^2]^{1/2}$, $r_2 = r$) is separated for $m = 0$ (at $d \longrightarrow \infty$). For $m \neq 0$ the term m^2/ρ^2 and, consequently, the Hamilto-

nian (23) is not separated in these coordinates. Note, for $m = 0$ the cases $\omega_z/\omega_\rho = 1/2$ and 2 are equivalent if we exchange the ρ and z coordinates and, hence, the additional integral of motion is $|a_\rho - \tilde\omega_z^2 z^2 \rho|$. For $m \neq 0$ we use the procedure described in [43] and obtain the following integral of motion

$$C = [(a_\rho - \tilde\omega_z^2 z^2 \rho)^2 + a_\varphi^2 + 4m^2\tilde\omega_z^2 r^2]^{1/2}, \qquad (36)$$

where a_ρ and a_φ are the ρ and φ components of the Runge–Lenz vector, respectively. Due to the existence of three independent integrals of motion, h, m, and c, which are in involution, the dynamics for $m \neq 0$, although non-separable, is integrable. The further analysis for $m = 0$ is similar to the previous one and we omit it here.

3.3. Diagonalization in Separable Cases

Let us denote by h^* the Hamiltonian (23) for a specific value of the magnetic field when the system becomes separable, i.e., for $\omega_L^* = \omega_L'$, ω_L'', or ω_L''' (for $m = 0$). Then for an arbitrary value of ω_L we can write

$$h = h^* + \frac{1}{2}\Delta\tilde\omega_L^2\rho^2 - \Delta\tilde\omega_L m, \qquad (37)$$

where $\Delta\tilde\omega_L^2 = \tilde\omega_L^2 - \tilde\omega_L^{*2}$, $\Delta\tilde\omega_L = \tilde\omega_L - \tilde\omega_L^*$ and the term $\frac{1}{2}\Delta\tilde\omega_L^2\rho^2$ is the only non-diagonal part of h in the eigenbasis of h^*. The eigenenergies of the Hamiltonian (23) (see Fig. 6) have been calculated with the use of the basis (35) and the spherical basis in the intervals $0 \leq \tilde\omega_L \leq 1.5$ and the $1.5 \leq \tilde\omega_L \leq 5$, respectively. The radial parts of the spherical eigenfunctions and $f_{n_1, n_2, m}$, as well as the corresponding factors in the matrix elements $\langle\psi_i|\rho^2|\psi_j\rangle$, are evaluated numerically. The complete spectrum of the two-electron QD (Fig. 6a) shows the accumulation of levels with different quantum numbers into well-pronounced bands in a strong magnetic field. There is no obvious manifestation of the symmetries discussed above. In fact, the effects of symmetries are shown for separated m-manifolds only (Fig. 6b).

For noninteracting electrons ($\lambda = 0$), the energy levels of the QD are Fock–Darwin levels [13]

$$\epsilon = \tilde\omega_\rho(2n_\rho + |m| + 1) + \tilde\omega_z\left(n_z + \frac{1}{2}\right) - \tilde\omega_L m. \qquad (38)$$

For rational ratios of ω_z/ω_ρ the energy levels Eq. (38) are degenerate. It is simply the spectrum of the RHO in the external field $\tilde\omega_L m$. For instance, at $\omega_z/\omega_\rho = 2$ we have $\epsilon = \tilde\omega_z(N + |m|/2 + 1) - \tilde\omega_L'' m$. The quantum number $N = n_\rho + n_z = n_1 + n_2 = 0, 1, 2, \dots$ and each m-manifold consists of the shells characterized by this quantum
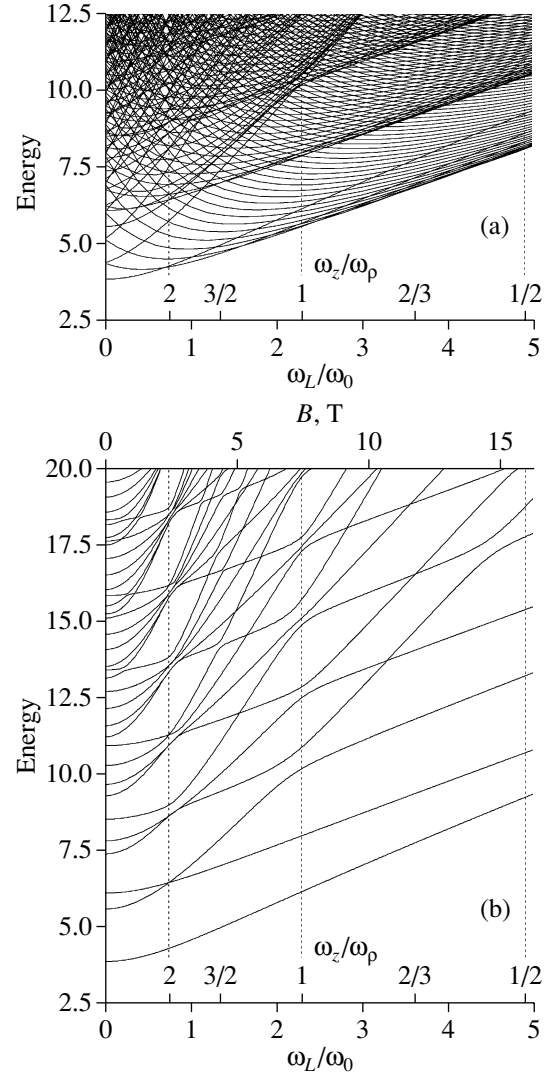

Fig. 6. The lowest eigenenergies of Hamiltonian (23) (in units $\hbar\omega_0$) at $\omega_z/\omega_0 = 2.5$ and $\lambda = 1.5$ as functions of the ratio ω_L/ω_0 for: (a) all m; (b) $m = 0$. The upper energy limit is chosen high enough to amplify the shell structure of the spectrum. The integrable cases: $\omega_z/\omega_\rho = 2$, 1, and 1/2 are indicated by vertical dotted lines ($\omega_L/\omega_0 = 0.75$, $\sqrt{21}/2$, and $\sqrt{24}$, respectively). From [40].

number. Since the eigenenergies of the term H_{CM} with the corresponding quantum numbers are determined by Eq. (21), which is the same as Eq. (38), the shells in the total spectrum of the QD are not affected.

4. DIMENSIONALITY EFFECTS IN GROUND-STATE TRANSITIONS OF TWO-ELECTRON QUANTUM DOTS

Two-electron quantum dots have drawn a great deal of experimental and theoretical attention in recent years [4, 7, 30]. Experimental data including transport measurements and spin oscillations in the ground state
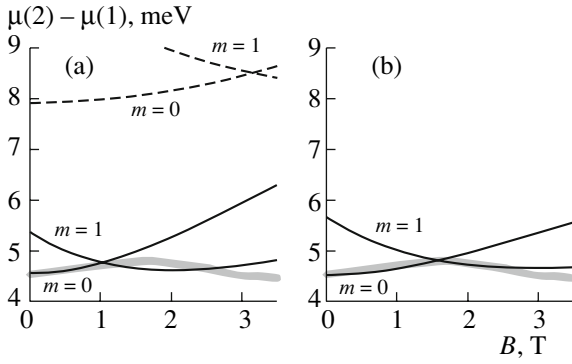
$\mu(2) - \mu(1)$, meV

Fig. 7. Difference $\Delta\mu$ of electro-chemical potentials, Eq. (40), from the experiment [47] (shaded curve). Part (a) shows the theoretical $\Delta\mu$ from a 2D quantum dot model with $\hbar\omega_0 = 5.4$ meV (dashed) and $\hbar\omega_0 = 2.3$ meV (solid). Part (b) shows $\Delta\mu$ from a 3D model with $\hbar\omega_0 = 2.6$ meV and $\omega_z/\omega_0 = 2.4$ (solid). From [39].

under a perpendicular magnetic field in two-electron QDs may be explained as a result of the interplay between electron correlations, a lateral confinement and magnetic field. In particular, one observes the transitions between states that can be characterized by different quantum numbers m and total spin S of Fock–Darwin states (see details in [47]). A 2D interpretation of experiments, however, leads to inconsistencies (see discussion in [4, 46]), providing, for example, too low values of the magnetic field for the first singlet-triplet (ST) transition. There is no consensus on the origin of this disagreement, since various experiments are dealing with different QDs. Evidently, it is important to understand the basic sources of such inconsistencies from a view point of possible technological applications, since QDs may provide a natural realization of quantum bit. This problem is also related to the fundamental aspects of strongly correlated *finite* systems, which are different from bulk and can be controlled experimentally.

4.1. The First Singlet-Triplet Transition in the Two-Electron QD

The ground state energy of a QD as a function of the magnetic field can be probed very elegantly by single electron capacitance spectroscopy (SECS) [47] or by single electron tunneling spectroscopy [48]. Applying a gate voltage to the contacts brings the electro-chemical potential of the contacts in resonance with the energy $\mu(N, B)$ necessary to add the Nth electron which tunnels through the barrier into the dot. We recall that the chemical potential of the dot is given by the ground state energy of the dot with N and $N - 1$ electrons (see Section 2),

$$\mu(N, B) = E(N, B) - E(N - 1, B). \quad (39)$$

Here, $E(N, B)$ denotes the total energy of the QD with N electrons under a magnetic field of strength B. Pres-

ently, we are concerned with $\mu(1, B)$ and $\mu(2, B)$ only, which we calculate with the aid of the model considered in Section 3 (see also [39]). The first is simply the harmonic oscillator energy for a single electron in the dot, $\mu(1, B) = E(1, B)$. The latter can be split into contributions from the relative and center-of-mass motion E_{CM}, where $E_{CM} = E(1, B)$. In our consideration the addition energy (direct probe of electron correlation in the dot) takes the form

$$\Delta\mu \equiv \mu(2, B) - \mu(1, B) = \hbar\omega_0\epsilon - E(1, B), \quad (40)$$

where ϵ is the relative energy determined by the Hamiltonian (23) and $E(1, B) = \omega_\rho + \hbar\omega_z/2$. Our aim is to describe the first singlet-triplet transition observed in two-electron QD under the perpendicular magnetic field [47].

In a number of papers (e.g., [47–50]) $\mu(1, B)$ has been used to estimate the confining frequency $\hbar\omega_0$ in a two-dimensional model of the QD. Indeed, with $\hbar\omega_0 = 5.4$ meV ($\hbar\omega_z = 0$) one obtains a very satisfactory fit to $\mu(1, B)$ (see [47]). However, with this $\hbar\omega_0$, neither $\Delta\mu$ (which is by almost a factor of two too large) nor the value for B, where the first singlet-triplet transition occurs, is reproduced correctly as is obvious from Fig. 7a. It has been argued that for an increasing magnetic field $\mu(N, B)$ might not follow the behavior modeled with a pure QD with a constant confining frequency, see [48, 50], and Ref. 11 in [49]. Hence, we believe it is more realistic to extract $\hbar\omega_0$ from the difference of the chemical potentials $\mu(2, 0) - \mu(1, 0)$ at zero magnetic field. This has been done in Fig. 7a and leads with $\hbar\omega_0 = 2.3$ meV ($\lambda = 1.66$) to the first singlet-triplet transition ($m = 0, S = 0$) $\Rightarrow$ ($m = 1, S = 1$) at $B = 1.02$ T (the Zeeman term is absent). This value differs from the experimental value of $B \approx 1.5$ T only by about 30% in contrast to the difference of more than a factor of two with $\hbar\omega_0 = 5.4$ meV (dashed line).

The discrepancy of 30% vanishes if one proceeds to a 3D description of the QD. In this case $\hbar\omega_0 = 2.6$ meV ($\lambda = 1.56$) is needed to match $\mu(2, 0) - \mu(1, 0)$, only slightly different from the 2D case, but the first singlet-triplet transition occurs now at $B = 1.59$ T (see Fig. 7b). If one includes the contribution from the Zeeman energy

$$E_Z = \frac{1}{2}\mu^* B[1 - (-1)^m] \quad (41)$$

with $\mu^* = g_L\mu_B$, $g_L = -0.44$, this value reduces to $B = 1.52$ T in a good agreement with the experiment. Of course, this agreement is achieved by tuning a second parameter, available in the 3D case, namely $\omega_z/\omega_0 = 2.4$, i.e., the ratio of vertical to lateral confinement. On the other hand, a rough estimate assuming $\omega_z/\omega_0 \sim d_0/d_z$ (see, for example [32]) reveals with the experimental value $d_z = 175$ Å, a lateral size of $d_0 \approx 420$ Å which is the correct order of magnitude, although the exact lateral extension in the experiment is not known [47]. The

analysis shows that in contrast to a 2D description, the 3D description provides a way to describe the energy spectrum for small B, the value of the magnetic field for the first singlet-triplet transition, and the ratio of the lateral to vertical extension of the dot consistently. To pursue discussion in favor of this view point we address the details of the recent study of excited states in two-electron vertical QDs [23].

It was predicted that the ground state of an N-electron QD becomes the spin polarized maximum density droplet (MDD) [51] at high magnetic fields. For a two-electron QD it is expected that the MDD occurs after the first ST transition (see discussion in [30]). Below we will demonstrate that the experimental results found in [23] related to the MDD can be explained if one takes into account the 3D physical nature of the QD. We will discuss the additional criterion to distinguish the 2D and 3D nature experimentally.

4.2. The Collapse of the MDD State in the Two-Electron QDs

Theoretical calculations [52] assert that after the first ST transition, the increase of the magnetic field induces several ground state transitions to higher orbital-angular and spin-angular momentum states. This issue was addressed in a transport study of the correlated two-electron states up to 8 and 10 T in lateral [53] and vertical [23, 24] QDs, respectively. It is quite difficult to detect the structure of ground states after the first ST transition in a lateral QD due to a strong suppression of the tunnel coupling between the QD and contacts. Altering the lateral confinement strengths, the transitions beyond the first ST transition are reported in vertical QDs [23]. In fact, the variation of the confining frequency with *the same experimental setup* opens a remarkable opportunity in the consistent study of the effects of the magnetic field on electron correlations.

Three vertical QDs with different lateral confinements have been studied in the experiment [23]. In all samples, the clear shell structure effects for an electron number $N = 2, 6, \ldots$ at $B = 0$ T have been observed, implying a high rotational symmetry. Although there is a sufficiently small deviation from this symmetry in sample C (from now on in accordance with the list of [23]), a complete shell filling for two and six electrons was observed. Such a shell structure is generally associated with a 2D harmonic oscillator $(x - y)$ confinement [4]. However, it is noteworthy that a similar shell structure is produced by a 3D axially symmetric HO if the confinement in the z-direction $\omega_z = 1.5\omega_0$ is only slightly larger than the lateral confinement ($\omega_x = \omega_y = \omega_0$). In this case six electrons fill the lowest two shells with Fock–Darwin energy levels with $n_z = 0$. It was also found that the lateral confinement frequency for the axially symmetric QD decreases with the increase of the electron number [54], since the screening in the lateral plane becomes stronger with a large

electron number. In turn, this effectively increases the ratio ω_z/ω_0 making the dot more "two-dimensional," since the vertical confinement is fixed by the sample thickness. Indeed, the N-dependence of the effective lateral frequency is observed in [23]. All these facts imply that the three-dimensional nature is a prerequisite of a consistent quantitative analysis of small QDs with a few electrons.

Our analysis is carried out by means of the exact diagonalization of the Hamiltonian (1) for two 3D interacting electrons in a perpendicular magnetic field. The confining potential in Eq. (1) is approximated by a 3D axially symmetric HO $U(\mathbf{r}) = m^*[\omega_0^2(x^2 + y^2) + \omega_z^2 z^2]/2$, where $\hbar\omega_z$ and $\hbar\omega_0$ are the energy scales of confinement in the z-direction and in the xy-plane, respectively. The evolution of the ground-state energy of a two-electron QD under the perpendicular magnetic field can be traced by means of the additional energy $\Delta\mu$ (see Eqs. (8), (39)).

Fitting the B-field dependence of the first and second Coulomb oscillation peak positions to the lowest Fock–Darwin energy levels of the 2D HO with the potential $m^*\omega_0^2 r^2/2$, Nishi et al. [23] estimated ω_0 for all three samples A, B, C. Although the general trend in the experimental data is well reproduced by the 2D calculations, the experimental positions of the ST transition points are systematically higher (see Fig. 3 of [23]). Different lateral confinements in the above experiment are achieved by the variation of the electron density, without changing the sample thickness. Using the "experimental" values for the lateral confinement and the confinement frequency ω_z as a free parameter, we found that the value $\hbar\omega_z = 8$ meV provides the best fit for the positions of kinks in the additional energy (40) with the Zeeman energy E_Z (41)

$$\Delta\mu = \hbar\omega_0\varepsilon - E(1, B) + E_Z \qquad (42)$$

in all three samples. Note that the Zeeman energy E_Z is zero for the singlet states. For the sake of illustration, we display in Fig. 8 the magnetic dependence of the experimental spacing between the first and the second Coulomb oscillation peaks $\Delta V_g = V_g(2) - V_g(1)$ for samples A–C, which can be transformed to the additional energy $\Delta\mu$ (see details in [23, 24]). In the $\Delta V_g - B$ plot, ground state transitions appear as upward kinks and shoulders [24]. It was found from the Zeeman splitting at high magnetic fields that $|g^*| = 0.3$ [24] and we calculate the additional energy with this and the bulk values.

We nicely reproduce the experimental position of the first ST transitions at $B = 4.2, 3, 2.3$ T in samples A, B, and C, respectively (see Fig. 8). When the magnetic field is low, a difference between the calculations with different $|g^*|$ factors is negligible. Upon decreasing the lateral confinement $\hbar\omega_0$ from sample A to sample C (the increase of the ratio ω_z/ω_0), the Coulomb interac-
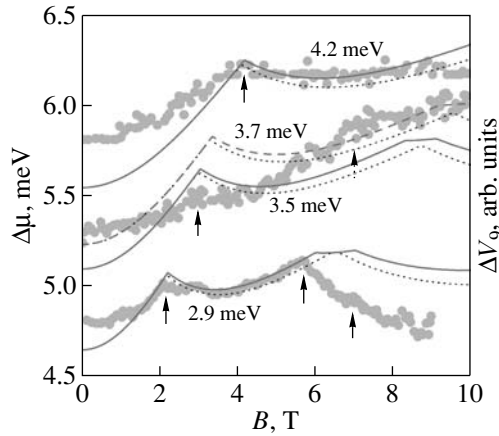
Fig. 8. The magnetic dependence of the additional energy $\Delta\mu$ in two-electron QDs with lateral confinements $\hbar\omega_0 = 4.2, 3.7, 3.5, 2.9$ meV (the first, second and fourth values are experimental values for sample A, B, and C, respectively [23]). The confinement in the third (z) direction $\hbar\omega_z = 8$ meV is fixed for all samples. The results for $|g^*| = 0.3(0.44)$ are connected by solid (dotted) line for $\hbar\omega_0 = 4.2, 3.5, 2.9$ meV and by dashed (dotted) line for $\hbar\omega_0 = 3.7$ meV. The solid grey lines display the experimental spacing ΔV_g as a function of B. The arrows identify the position of experimental ground state transitions [23]. From [55].

Fig. 9. Magnetic field dependence of the addition energy $\Delta\mu$ for the 2D model with $\hbar\omega_0 = 2.9, 3.5$ meV and for the 3D model ($\hbar\omega_0 = 2.9$ meV, $\hbar\omega_z = 8$ meV). Ground states are labeled by (M, S), where M and S are the total orbital momentum and the total spin, respectively. Grey vertical lines indicate the position of the experimental crossings between different ground states. From [55].

tion becomes dominant in the interplay between electron correlations and the confinement [39]. In turn, the smaller the lateral confinement at a fixed thickness (the stronger the electron correlations), the smaller the value of the magnetic field, at which the ST transitions or, in general, crossings between excited states and the ground state may occur.

There is no signature for the second crossing in the ground state for sample A at large B (up to 10 T). Here, the ratio $\omega_z/\omega_0 \approx 1.9$ and the effect of the third dimension is most visible: the confinement has a dominant role in the electron dynamics and a very high magnetic field is required to observe the next transition in the ground state due to electron correlations. Thus, the MDD phase survives until very high magnetic fields ($B \sim 10$ T).

A second kink is observed at $B = 7$ T in sample B [23]. Our calculations with the "experimental" lateral confinement $\hbar\omega_0 = 3.7$ meV produces the second kink at $B = 9.5$ T, which is located higher than the experimental value. The slight decrease of the lateral frequency until $\hbar\omega_0 = 3.5$ meV shifts the second kink to $B = 8.7$ T, improving the agreement with the experimental position of the first ST transition as well. In addition, the use of $|g^*| = 0.3$ (instead of the bulk value) with the latter frequency creates a plateau, which bears resemblance to the experimental spacing ΔV_g. However, there is no detailed information on this sample and we lack a full understanding of this kink. It seems there is an additional mechanism responsible for the second kink in sample B.
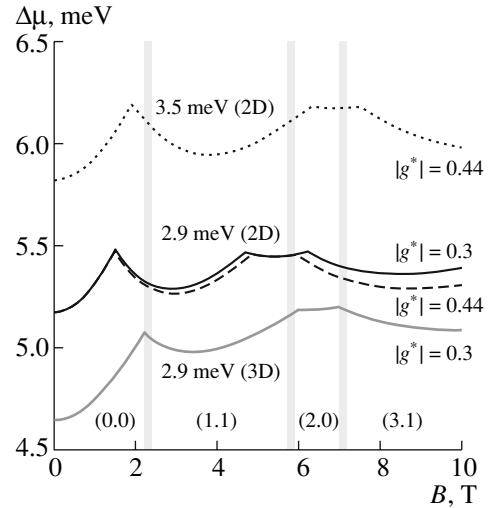
The most complete experimental information is related to sample C and we also study this sample in detail. In sample C the first experimental ST transition occurs at $B = 2.3$ T, while the signatures of the second and the third ones are observed at $B \approx 5.8, 7.1$ T, respectively (see Fig. 8). The 2D calculations (with the "experimental" values $\hbar\omega_0 = 2.9$ meV, $|g^*| = 0.44$) predict the first, second and third ST crossings at lower magnetic fields: $B = 1.7, 4.8, 5.8$ T, respectively (see Fig. 9). The results can be improved to some degree with $|g^*| = 0.3$. To reproduce the data for $\Delta\mu$ Nishi et al. [23] have increased the lateral confinement ($\hbar\omega_0 = 3.5$ meV, $|g^*| = 0.44$). As a result, the first, second and third ST transitions occur at $B = 2, 6.3, 7.5$ T, respectively. Evidently, 2D calculations overestimate the importance of the Coulomb interaction. The increase of the lateral confinement weakens simply the electron correlations in such calculations. In contrast, the 3D calculations reproduce the positions of all crossings with the "experimental" lateral confinement $\hbar\omega_0 = 2.9$ meV at $B = 2.3, 5.8, 7.1$ T (see Fig. 9) very well.

One of the questions addressed in the experiment [23] is related to a shoulderlike structure observed in a small range of values for the magnetic field (see our Figs. 8 and 4 of [23]). This structure is identified as the second singlet state (2, 0) that persists until the next crossing with the triplet state (3, 1). According to [23], the ground state transition from the triplet (1, 1) state to the singlet (2, 0) is associated with the collapse of the MDD state for $N = 2$. Therefore, a question arises: at which conditions it would be possible to avoid the collapse of the MDD phase (in general, to preserve the
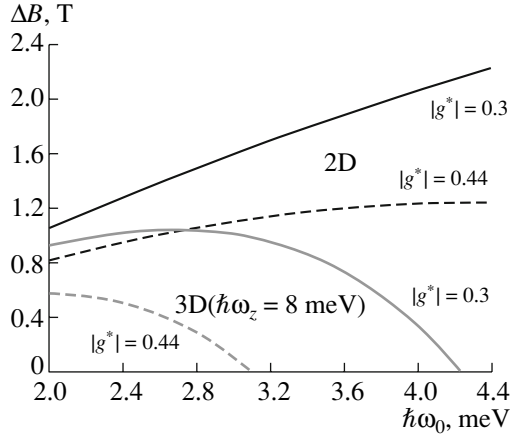
Fig. 10. The interval ΔB in which the singlet state $(2, 0)$ survives as a function of the lateral confinement for 2D and 3D calculations. The confinement in the third (z) direction $\hbar\omega_z = 8$ meV is fixed for the 3D calculations. From [55].

Fig. 11. Top: the magnetic dependence of the ground state in 2D and 3D ($\hbar\omega_z = 8$ meV) approaches for a lateral confinement $\hbar\omega_0 = 2$ meV. The 2D (left) and 3D (right) electron densities are displayed for different ground states (M, S) at corresponding magnetic fields. The largest 3D density grows from a central small core over a ring to a torus with the increase of the magnetic field. From [55].

spin-polarized state); i.e., at which conditions the singlet $(2, 0)$ state will never show up in the ground state. In fact, the collapse of the MDD depends *crucially* on the value of the lateral confinement and *the dimension* of the system. We found that in the 2D consideration the $(2, 0)$ state always exists for experimentally available lateral confinement (see Fig. 10). Moreover, in this range of ω_0 the 2D approach predicts the monotonic increase for the interval of values of the magnetic field ΔB, at which the second singlet state survives, with the increase of the lateral confinement. In contrast, in the 3D calculations, the size of the interval is a vanishing function of the lateral confinement for a fixed thickness ($\hbar\omega_z = 8$ meV). It is quite desirable, however, to measure this interval in order to draw a definite conclusion and we hope it will be done in future.

As discussed above, the decrease of the confinement at fixed thickness increases the dominance of the electron correlations in the electron dynamics. Furthermore, this decrease, related to the decrease of the electron density [54, 23], creates the favorable conditions for the onset of electron localization. This localization (crystallization) in QDs is associated with the formation of the so-called Wigner molecule [56]. In the 2D approach the crystallization is controlled by the ratio of Coulomb and confinement strengths $\lambda = (k/l_0)/\hbar\omega_0 \equiv R_W$ ($l_0 = (\hbar/m^*\omega_0)^{1/2}$) (cf. [57]), which is about $R_W \sim 3$ for the QDs considered in experiments [23]. For a 2D two-electron QD, it is predicted that the Wigner molecule can be formed for $R_W \sim 200$ at a zero magnetic field [58], or at a very high magnetic field [59] (for $\hbar\omega_0 \sim 3$ meV and small R_W such as in the experiments [23]). In the 3D axially symmetric QDs the ratio between vertical and lateral confinements (anisotropy) may, however, affect the formation of the Wigner molecule. This problem can be analyzed by a dint of the electron density
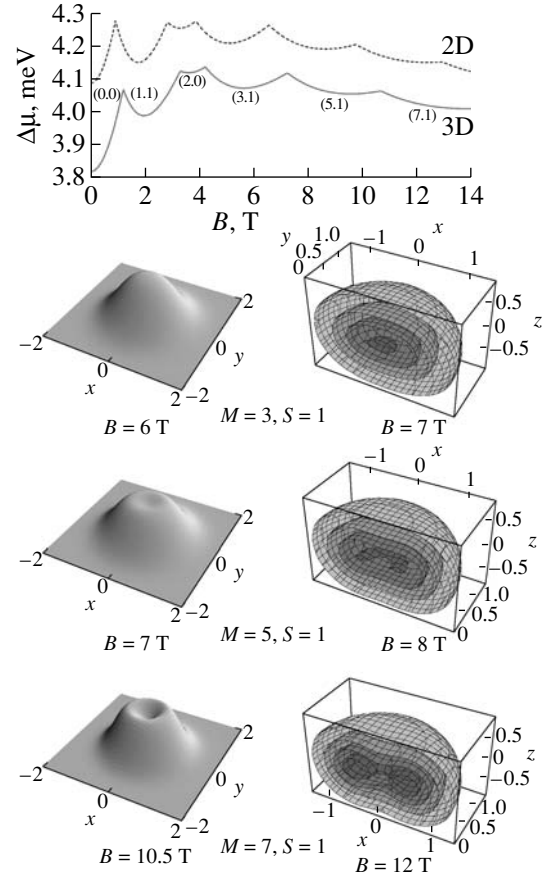
$$n(\mathbf{r}) = \int [|\Psi(\mathbf{r}, \mathbf{r}')|^2 + |\Psi(\mathbf{r}', \mathbf{r})|^2] d\mathbf{r}', \qquad (43)$$

when one electron is at the position $\mathbf{r}$ if the other one is located at a position $\mathbf{r}'$. A criterion for the onset of the crystallization in QDs can be the appearance of a local electron density minimum at the center of the dot [60]. For 2D QDs this leads to a radial modulation in the electron density, resulting in the formation of rings and roto-vibrational spectra [61].

Our analysis of the conditions realized in the experiments [23] predicts very high magnetic fields ($B > 12$ T) for the formation of the Wigner molecule. However, with a slight decrease of the lateral confinement, at $\hbar\omega_0 = 2$ meV we obtain the desired result. The 3D analysis of electron density (see Fig. 11) gives an unequivocal answer that at $B > 7.25$ T the triplet state $(5, 1)$ can be associated with a formation of the Wigner molecule. There is an evident difference between the 2D and 3D approaches: the 2D calculations predict the crystallization at a lower magnetic field ($\Delta B \sim 1$ T). The further
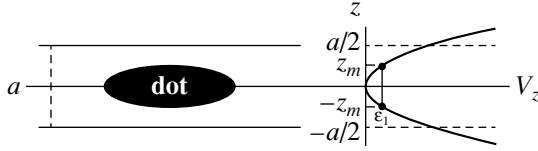
Fig. 12. Left: the localization of QD in the layer of the thickness a. Right: the schematic representation of the position of zero-point motion in the parabolic confinement relative to the layer thickness.

increase of the magnetic field leads to the formation of a ring and a torus of maximal density in 2D- and 3D-densities, respectively. Note that if geometrical differences are disregarded, 3D evolution of the ground state can be approximately reproduced in the 2D approach with the effective charge concept [39] (see also [53]). This problem will be discussed in the Section 5.

5. EFFECTIVE CHARGE

It is self-evidently true that in QDs the Coulomb interaction couples lateral and vertical coordinates and the problem is non-separable, in general. By virtue of the exact diagonalization of the 3D effective Hamiltonian one can study the effect of the vertical confinement on the energy spectrum (cf. [54]). This can be done, however, only for QDs with a small number of electrons. Even in this case there are difficulties related to the evaluation of 3D interaction matrix elements. The problem simplifies significantly if it is possible to separate the center of mass motion from the relative motion like in the fully parabolic potential. It is the purpose of the present section to introduce a consistent approach which enables us to reduce a 3D Coulomb problem to the 2D one without losing major effects related to the QD's thickness for an arbitrary vertical confinement.

In real samples the confining potential in the z-direction is much stronger than in the xy-plane. It results in different time scales (see below) and this allows one to use the adiabatic approach [62]. To account for the effect of localization of the dot in the layer of thickness a, let us consider a 3D model for two electrons described by the Hamiltonian (1) with a potential $U(\mathbf{r}) = m^*[\omega_0^2(x^2 + y^2) + \omega_z^2 z^2]/2$, where $\hbar\omega_z$ and $\hbar\omega_0$ are the energy scales of confinement in the z-direction and in the xy-plane, respectively. The thickness of QDs is much smaller in comparison with the lateral extension. Therefore, the vertical confinement $\hbar\omega_z$ is much stronger then the lateral confinement $\hbar\omega_0$ and this fact is, usually, used to justify a 2D approach for the study of QDs. However, there is a nonzero contribution from the vertical dynamics, since the energy level available for each of the noninteracting electrons in z-direction is $\varepsilon = \hbar\omega_z(n_z + 1/2)$. For the lowest state $n_z = 0 \Rightarrow \varepsilon_1 =$

$\frac{1}{2}\hbar\omega_z$. By dint of the condition $V_z(\pm z_m) \equiv m^*\omega_z^2 z_m^2/2 = \varepsilon_1$ one defines the turning points: $z_m = \sqrt{\hbar/(m^*\omega_z)}$. We assume that the distance between turning points should not exceed the layer thickness, i.e., $2z_m \le a$ (see Fig. 12). In virtue of this inequality it follows that the lowest limit for the vertical confinement in the layer of thickness a is

$$\hbar\omega_z \ge \frac{4\hbar^2}{m^*a^2} \tag{44}$$

For typical GaAs samples with the thickness a between 10 and 20 nm this estimation gives the minimal value for $\hbar\omega_z$ between 45 and 11 meV, respectively. These estimations provide a genuine reason for the use of the adiabatic approach in case of QDs, since $T_z(=2\pi/\omega_z) \ll T_0(=2\pi/\omega_0)$.

5.1. Adiabatic Approximation

To the lowest order the adiabatic approach consists of averaging the full 3D Hamiltonian (1) over the angle-variables $\theta_{z_i} = \omega_{z_i}t$ (fast variables) of the unperturbed motion ($k = 0$) of two electrons after rewriting the (z_i, p_{z_i}) variables in terms of the action-angle variables (J_{z_i}, θ_{z_i}). As a result, the dynamics effectively decouples into an unperturbed motion in the vertical direction governed by the potential $\sum_i V(J_{z_i}, \theta_{z_i})$ and into the lateral motion governed by the effective potential

$$V_{\text{eff}}(\{x, y\}; \{J_z\}) = \sum_i v_i + V_C^{\text{eff}}(\rho; J_{z_1}, J_{z_2}), \tag{45}$$

where v is defined below in Eq. (48) and

$$V_C^{\text{eff}}(\rho; J_{z_1}, J_{z_2})$$

$$= \frac{1}{(2\pi)^2}\int_0^{2\pi}d\theta_{z_1}\int_0^{2\pi}d\theta_{z_2}V_C(\rho, z_1(J_{z_1}, \theta_{z_1}) - z_2(J_{z_2}, \theta_{z_2})) \tag{46}$$

is the effective electron-electron interaction that contains the memory on z dynamics through integrals of motion J_{z_i}. The effective electron-electron interaction affects, therefore, only the dynamics in the lateral plane, where the confining potential is the parabolic one. Hence, the effective Hamiltonian for two-electron QD reads

$$H_{\text{eff}} = H_0 + E_z + V_C^{\text{eff}}, \tag{47}$$

where $E_z = \sum_i \varepsilon_i$ and ε_i is the electron energy of the unperturbed motion in the vertical direction. The term $H_0 = \sum_{i=1}^2 h_i$ consists of the contributions related only

to the lateral dynamics (*xy*-plane) of noninteracting electrons

$$h = t + v - \omega_L l_z$$

$$= \frac{p_\rho^2}{2m^*} + \left(\frac{l_z^2}{2m^*\rho^2} + \frac{1}{2}m^*\omega_\rho^2\rho^2 \right) - \omega_L l_z. \tag{48}$$

We recall that the effective lateral confinement frequency $\omega_\rho = (\omega_0^2 + \omega_L^2)^{1/2}$.

Our approach is based on the transparent physical idea that the third dimension reduces the Coulomb interaction in comparison with the 2D case. Therefore, our proposal consists in the consideration of the Coulomb term determined by the effective value k_{eff} ("effective charge") with due regard of the vertical (z) dynamics, i.e.,

$$V_C = \frac{k}{r_{12}} \approx \frac{k_{\text{eff}}}{\rho}, \tag{49}$$

where $\rho = [(x_1 - x_2)^2 + (y_1 - y_2)^2]$. In order to evaluate the effective charge, let us present the effective Coulomb term (46) in the following form $V_C^{\text{eff}} = kf(\rho)/\rho$. Then one can define the effective charge as the mean value of the function $kf(\rho)$. As we will see below this approach provides a remarkable agreement with the 3D theory.

Thus, the procedure for evaluating the effective charge consists of two steps: (i) the averaging of the Coulomb term $V_C(\rho, z)$ over the angle variables in the z-direction, which gives the effective 2D potential $V_C^{\text{eff}}(\rho) = kf(\rho)/\rho$; (ii) the calculation of the mean value of the factor $f(\rho)$ upon the nonperturbed lateral wave functions, i.e.,

$$k_{\text{eff}} = k\langle f(\rho) \rangle \equiv \langle \rho V_C^{\text{eff}}(\rho) \rangle. \tag{50}$$

For a parabolic (lateral) confinement, the nonperturbed wave functions are Fock–Darwin states (cf. [3]). Due to the Kohn theorem [14] (see Sections 1, 3 and below), the mean value in Eq. (50) can be evaluated using the Fock–Darwin states for the relative motion. For the lowest states (with different values of the quantum number m related to the z-component of orbital momentum but with the radial quantum number $n_\rho = 0$) one obtains for the effective charge

$$k_{\text{eff}} = \frac{2}{|m|!} \left(\frac{\mu\omega_\rho}{\hbar} \right)^{|m|+1} \int_0^\infty e^{-\mu\omega_\rho\rho^2/\hbar} \rho^{2|m|+2} V_C^{\text{eff}}(\rho) d\rho, \tag{51}$$

where $\mu = m^*/2$ is the reduced mass.

5.2. Parabolic Potential

As it was discussed in Section 3, in the 3D model with a vertical confinement approximated by a para-

bolic potential the CM and the relative motions are separated. Since the CM dynamics does not affect the electron interaction, we consider only the 3D Hamiltonian for the relative motion

$$H_{\text{rel}} = h_{\text{rel}} + \frac{k}{r} + \frac{p_z^2}{2\mu} + \frac{\mu\omega_z^2 z^2}{2}. \tag{52}$$

The term h_{rel} is defined by Eq. (48) in which the effective electron mass is replaced by the reduced mass μ; $\mathbf{r} = \mathbf{r}_1 - \mathbf{r}_2$ (ρ, p_ρ) are the relative coordinates and l_z is the z-projection of the angular momentum for relative motion [39].

After rewriting the (z, p_z) variables in terms of the action-angle variables (J_z, θ_z)

$$z = \sqrt{\frac{2J_z}{\mu\omega_z}} \sin\theta_z, \quad p_z = \mu\dot{z} \tag{53}$$

for the unperturbed ($k = 0$) motion (see details in Appendix A in [39]), one has to integrate out of the fast variable, i.e., average the Hamiltonian (52) over the angle θ_z. As a result, the effective electron-electron interaction is (see Appendix B in [39])

$$V_C^{\text{eff}}(\rho; J_z) = \frac{2k}{\pi\rho} K\left(-\frac{2J_z}{\mu\omega_z\rho^2} \right), \tag{54}$$

where $K(x)$ is the complete elliptic integral of the first kind. The effective Hamiltonian for the relative motion is

$$H_{\text{rel}}^{\text{eff}} = h_{\text{rel}} + V_C^{\text{eff}}(\rho; J_z) + E_z^{\text{rel}} \tag{55}$$

$$E_z^{\text{rel}} = \omega_z J_z = \hbar\omega_z(n_z + 1/2). \tag{56}$$

Taking into account the definitions of Eqs. (50), (56) and the result Eq. (54), one obtains for the effective charge

$$k_{\text{eff}} = \frac{2k}{\pi} \left\langle n_\rho, m \left| K\left(-\frac{\hbar(2n_z + 1)}{\mu\omega_z\rho^2} \right) \right| n_\rho, m \right\rangle, \tag{57}$$

where $|n_\rho, m\rangle$ are the Fock–Darwin states (see Eq. (A.9) in Appendix A; for the relative motion $n_\rho = n_r$, $\omega_\rho = \Omega$, $m^* \Rightarrow \mu$).

For the lowest states ($n_\rho = n_z = 0$) one reduces Eq. (57) to the form of integral (51). As a result, the effective charge can be expressed in terms of the Meijer G-function [63]

$$k_{\text{eff}} = \frac{k}{\pi|m|!} G_{2,3}^{2,2}\left(\frac{\omega_\rho}{\omega_z} \left| \begin{matrix} 1/2 & 1/2 \\ 0 & m+1 & 0 \end{matrix} \right. \right). \tag{58}$$

Guided by the adiabatic approach, it is instructive to compute the effective charge by a dint of the quantum-mechanical mean value of the Coulomb term in the 3D oscillator state $|n_\rho, m\rangle|n_z\rangle$

$$k_{\text{eff}} = \langle\langle \rho V_C(\rho, z) \rangle\rangle = k\langle\langle (1 + z^2/\rho^2)^{-1/2} \rangle\rangle. \tag{59}$$
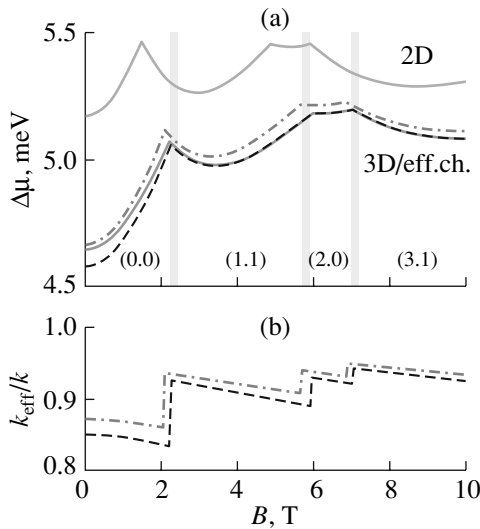
Fig. 13. (a) The additional energy $\Delta\mu$ as a function of the magnetic field in the parabolic model. The results of calculations with a lateral confinement only (the 2D approach, $\hbar\omega_0 = 2.9$ meV, $|g^*| = 0.3$) and full 3D approach [55] ($\hbar\omega_z = 8$ meV) are connected by solid (——) and (——) lines, respectively. The vertical grey lines indicate the position of the experimental crossings between different ground states in a sample C [23]. Ground states are labeled by (m, S), where m and S are the quantum numbers of the operators l_z and the total spin, respectively. The results based upon the adiabatic approximation, Eq. (58), and the plain quantum-mechanical averaging procedure, Eq. (60), are connected by dashed (– – –) and dot-dashed (– · –) lines, respectively. (b) The ratio k_{eff}/k as functions of the magnetic field based on Eq. (58) and the plain quantum-mechanical averaging, Eq. (60) are connected by dashed (– – –) and dot-dashed (– · –) lines, respectively.

In this case the adiabatic approach is determined by the ratio $(z/\rho)^2$.

This ratio is a naturally small parameter of theory, since the lateral extension exceeds the thickness of the QDs by several times. For $n_\rho = n_z = 0$ one obtains

$$
k_{eff} = k\frac{2}{|m|!}\left(\frac{\mu\omega_\rho}{\hbar}\right)^{|m|+1}\sqrt{\frac{\mu\omega_z}{\pi\hbar}}
$$
$$
\times\int_0^\infty K_0\left(\frac{\mu\omega_z\rho^2}{2\hbar}\right)e^{\mu\left(\frac{1}{2}\omega_z-\omega_\rho\right)\rho^2/\hbar}\rho^{2|m|+2}d\rho, \tag{60}
$$

where K_0 is the modified Bessel function of the second kind. One observes that in both definitions of the effective charge in Eqs. (57), (60) there is a contribution of the electron dynamics along the coordinate z.

5.3. Comparison of Different Approaches

To illuminate the key advantage of the effective charge concept it is noteworthy to analyze the available experimental data [23] within various approaches. To this aim we will compare the results of the calculations

of the additional energy in 2D approximation (with the effective Coulomb interaction) and in the 3D approach with a full Coulomb interaction.

As it was shown above, using the "experimental" values for the lateral confinement [23] and the confinement frequency ω_z as a free parameter, we successfully reproduced with the value $\hbar\omega_z = 8$ meV and $|g^*| = 0.3$ the positions of kinks in the additional energy in all three samples [55]. In other words, we were able to reproduce all experimental singlet-triplet transitions in the ground states of the two-electron vertical QDs, induced by the magnetic field [23]. We recall that in the 2D approach used by Nishi et al. [23] one encounters the problem of the correct interpretation of the experimental data (see, for example, Fig. 13a, a plain lateral confinement $\hbar\omega_0 = 2.9$ meV). In the effective charge approximation the vertical confinement is taken into account with the aid of k_{eff} in the 2D effective Hamiltonian. The remarkable accord between the predictions based on our results and the observation confirms the validity of the suggested concept (see Fig. 13).

Note that the results based upon the adiabatic approximation are in a better agreement with the full 3D calculations in contrast to those obtained with the aid of the plain quantum-mechanical averaging procedure for $k_{eff} = \langle\langle\rho V_C(\rho, z)\rangle\rangle$. As discussed above, the adiabatic approach is based on the effective separation of fast (vertical) and slow (lateral) dynamics with a subsequent averaging procedure. In contrast, the plain quantum-mechanical averaging represents a type of perturbation theory based upon the first order contribution with respect to the ratio z/ρ only. The higher order term may improve the agreement at a small magnetic field, since the vertical dynamics is non negligible and affects the lateral dynamics. The increase of the quantum number m, caused by the increase of the magnetic field strength, reduces the orbital motion of electrons in the vertical direction. The larger the m the stronger the centrifugal forces, which induce the electron localization in a plane, and, therefore, the lesser the importance of the vertical electron dynamics. In the limit of a strong magnetic field (large m) the dot becomes more of a "two-dimensional" system. This explains the improvement of the accuracy of the plain quantum-mechanical averaging procedures at large m, i.e., for the ground states at high magnetic fields.

Finally, a remark is in order. For the sake of illustration we have used only k_{eff} for the lowest basis states ($n_\rho = n'_\rho = 0$) with different m. However, even for the ground state calculations with the aid of the exact diagonalization, the interaction matrix elements $k_{eff}\langle n'_\rho, m|\rho^{-1}|n'_\rho, m\rangle$ with $n_\rho, n'_\rho \geq 0$ have been taken into account. Namely, the diagonalization is performed using the interaction matrix elements up to $n_\rho, n'_\rho = 10$. Obviously, the accuracy of the method would improve if one calculates the "effective charge matrix elements"

$k_{n_\rho, n'_\rho}^{(m)} = \langle n'_\rho, m | \rho V_C^{\text{eff}} | n'_\rho, m \rangle$ for each interaction matrix element. However, in this case the procedure would lose the simplicity and becomes impractical. Fortunately, from the comparison of the present results with exact 3D calculations we found that for the analysis of the ground state properties it is sufficient to use only the elements $k_{0,0}^{(m)} \equiv k_{\text{eff}}^{(m)}$, even for the interaction matrix elements with n_ρ, $n'_\rho \geq 0$.

CONCLUSION

The consequences of shell structure effects for the addition energy of a small isolated quantum dot for noninteracting electrons have been analyzed in a simple model with a parabolic confinement [26, 32]. At certain values of the magnetic field strength shell structures appear in a spectrum of a quantum dot, also in cases where deformation does not give rise to magic numbers at a zero field strength. Measurements of the magnetic susceptibility are expected to reflect the properties of the single-particle spectrum and should display characteristic patterns depending on the particle number [33].

We have shown that quantum spectra obtained in the model of the axially symmetric 3D quantum dot with two interacting electrons exhibit hidden symmetries at certain values of the magnetic field. The Coulomb interaction destroys the general symmetry of the 3D HO. However, the magnetic field can recover symmetries, which are common for the RHO and Coulomb systems. At a relatively low value of the magnetic field ω_L'' (for our parameters $B \approx 2.4$ T) we reveal the first manifestation of the hidden symmetries in two-electron QD. This symmetry is determined by the integral of motion, Eq. (32). It results in the appearance of shells at each m-manifold (Fig. 6b). There are exact crossings and repulsions between levels of different and of the same parity, respectively, in each shell. The near-degeneracy of the quantum spectrum is reminiscent of a striking degeneracy observed for the RHO or pure Coulomb systems. At higher values of the magnetic field ω_L' ($B \approx$ 7.5 T), the dynamic spherical symmetry appears, since $\mathbf{l}^2$ becomes an additional integral of motion. This symmetry manifests itself as the attraction between levels with different orbital quantum numbers and the same parity (Fig. 6b). In contrast to spectra of pure Coulomb systems or of the RHO, there are no crossings between eigenstates of the subset characterized by a given quantum number m, since the accidental degeneracy is removed. Although the symmetry is recovered at a very strong magnetic field ω_L''' ($B \approx 15.9$ T) due to the appearance of the integral of motion Eq. (36), the dynamics is non-separable for $m \neq 0$. Note that shells are similar to the spherical case.

The symmetries may be detected by studying the conductance of two-electron QDs at low temperatures.

In particular, at ω_L'' in the excited states there is the onset of a singlet-triplet degeneracy related to the crossings of the eigenstates (35) with $|c| > 0$ (see Fig. 6b). The total spin S alternates between 1 and 0 and the addition of a second electron with a spin-up or spin-down orientation to the QD will cost the same energy.

We demonstrated that the confinement in the z direction is an important ingredient for the quantitative analysis of the experimental data for two-electron axially symmetric vertical QDs. In contrast to the 2D description, the 3D approximation provides a consistent description for various experimental features: the energy spectrum for a small magnetic field, the value of the magnetic field for the first and the second singlet-triplet transitions. We propose a criterion for the additional spectra, which evidently demonstrates the effect of the third dimension. According to this criterion the singlet state (2, 0) is a vanishing function of the lateral confinement (see Fig. 10) in the vertical magnetic field in the two-electron axially symmetric vertical QD. We found that the decrease of the lateral confinement in the experiment [23] until $\hbar\omega_0 = 2$ meV would lead to the formation of the Wigner molecule at $B \sim 8$ T.

We developed the effective charge approach taking full account of the thickness of two-electron quantum dots. Our approach is based on the adiabatic approximation where the full 3D dynamics of two interacting electrons is separated by means of action-angle variables on the independent vertical motion and the lateral dynamics described by the effective 2D Hamiltonian. The separations are reached due to a different time scale in the vertical (fast) and lateral (slow) dynamics and it is well justified in all types of QDs (vertical and lateral). As a result, one has to only solve the Schrödinger equation for 2D effective Hamiltonian where the full charge k is replaced by k_{eff} (*screened Coulomb interaction*) (see Eqs. (50), (51)). The eigenvalue problem was solved by a dint of the exact diagonalization of the effective 2D Hamiltonian in the Fock–Darwin basis. The screening due to the sample thickness is especially strong for quantum states with small values of the quantum number m. We recall that these states determine the structure of ground state transitions at small and intermediate values for the magnetic field. Therefore, the screening provides a consistent way to deal with the effect of the thickness upon the position of the singlet-triplet transitions. In particular, the screening should be taken into account for the analysis of evolution for the energy difference between singlet and triplet states in the magnetic field. This energy is considered to be important for analysis of the entanglement and concurrence in QDs (cf. [64]). The comparison of the results with the available experimental data [23] demonstrates a remarkable agreement and confirms the vitality of the approach. Being important for the states with a small quantum number m, the screening of the Coulomb interaction becomes small for the states with large m, which dominate in low-lying

spectrum at large magnetic fields. On the other hand, these states cause strong centrifugal forces, which induce the electron localization in a plane. In turn, the stronger the magnetic field the less important the vertical confinement. It follows that a plain Coulomb interaction becomes reliable in 2D approaches for the analysis of the ground state evolution of QDs only at very large magnetic fields. Finally, we would like to stress that, while this approach facilitates calculations, the effects related to the hidden symmetries can be understood only in the 3D approximation.

APPENDICES

APPENDIX A

TWO-DIMENSIONAL HARMONIC OSCILLATOR IN A PERPENDICULAR MAGNETIC FIELD

The electronic spectrum generated by the Hamiltonian (1) without interaction is determined by a sum $\sum_i^N h_i$ of a single-particle harmonic oscillator Hamiltonians $h = h_0 + h_z$ (see Section 2). The properties of the Hamiltonian h_z are well known [41]. The eigenvalue problem for the Hamiltonian h_0 can be solved using the transformation

$$\begin{pmatrix} x \\ y \\ V_x \\ V_y \end{pmatrix} = \begin{pmatrix} X_+ & X_+^* & X_- & X_-^* \\ Y_+ & Y_+^* & Y_- & Y_-^* \\ V_x^+ & V_x^{+*} & V_x^- & V_x^{-*} \\ V_y^+ & V_y^{+*} & V_y^- & V_y^{-*} \end{pmatrix} \begin{pmatrix} a_+ \\ a_+^\dagger \\ a_- \\ a_-^\dagger \end{pmatrix}. \quad (A.1)$$

Here, a_i^+ (a_i) is a creation (annihilation) operator of a new mode $i = \pm$ with the following commutation relations

$$[a_i, a_j^+] = \delta_{i,j}, \quad [a_i, a_j] = [a_i^\dagger, a_j^\dagger] = 0. \quad (A.2)$$

One can solve equation of motion

$$[a_i, h_0] = \Omega_i a_i, \quad i = \pm \quad (A.3)$$

and express the Hamiltonian h_0 through new normal modes

$$h_0 = \hbar\Omega_+(a_+^\dagger a_+ + 1/2) + \hbar\Omega_-(a_-^\dagger a_- + 1/2), \quad (A.4)$$

where

$$\Omega_\pm^2 = \frac{1}{2}(\omega_x^2 + \omega_y^2 + 4\omega_L^2$$

$$\pm \sqrt{(\omega_x^2 - \omega_y^2)^2 + 8\omega_L^2(\omega_x^2 + \omega_y^2) + 16\omega_L^4}). \quad (A.5)$$

The eigenstates of the Hamiltonian h_0 are

$$|n_+ n_-\rangle = \frac{1}{\sqrt{n_+! n_-!}}(a_+^+)^{n_+}(a_-^+)^{n_-}|00\rangle. \quad (A.6)$$

The operator l_z is diagonal in this basis

$$l_z = n_- - n_+. \quad (A.7)$$

In case of circular symmetry, i.e., $\omega_x = \omega_y = \omega_0$, the eigenstate Eq. (A.6) reduces to the form of the Fock–Darwin state (see [3]). Quite often it is useful to use the representation of the Fock–Darwin state in cylindrical coordinates (ρ, θ), which has the form

$$\phi_{n_r m}(\rho, \theta) = \frac{1}{\sqrt{2\pi}}\exp^{im\theta} R_{n_r m}(\rho). \quad (A.8)$$

This state is eigenfunction of the operator l_z with eigenvalue m and the radius-dependent function has the form

$$R_{n_r m}(\rho) = \frac{\sqrt{2}}{l_0^B}\sqrt{\frac{n_r!}{(n_r + |m|)!}}\left(\frac{\rho}{l_0^B}\right)^{|m|}$$

$$\times \exp\left[-\frac{\rho^2}{2l_0^{B^2}}\right]\mathcal{L}_{n_r}^{|m|}\left(\frac{\rho^2}{l_0^{B^2}}\right). \quad (A.9)$$

Here $l_0^{B^2} = \hbar/(2m^*\Omega)$, $\Omega = \sqrt{\omega_0^2 + \omega_L^2}$ and $\mathcal{L}$ denotes the Laguerre polynomials [41].

The pair of quantum numbers (n, m) and (n_+, n_-) are related by

$$n = n_+ + n_-, \quad m = n_- - n_+ \quad (A.10)$$

and $n = 2n_r + |m|$. The single-particle energy in the Fock–Darwin state is

$$\varepsilon(n, m) = \hbar\Omega(n + 1) - \hbar\omega_L m$$

$$= \hbar\Omega(2n_r + |m| + 1) - \hbar\omega_L m. \quad (A.11)$$

The quantum number n is associated with a shell number N_{sh} for an N-electron quantum dot in 2D approach.

APPENDIX B

THE RUNGE–LENZ VECTOR

The components of the Runge–Lenz vector $\mathbf{a} = \mathbf{p} \times \mathbf{l} + \lambda\mathbf{r}/r$ in (scaled) cylindrical coordinates are

$$a_\rho = (\rho p_z - z p_\rho)p_z + \left(\frac{m^2}{\rho^2} + \frac{\lambda}{r}\right)\rho,$$

$$a_\varphi = -\frac{m}{\rho}(\rho p_\rho + z p_z), \quad (B.12)$$

$$a_z = (z p_\rho - \rho p_z)p_\rho + \left(\frac{m^2}{\rho^2} + \frac{\lambda}{r}\right)z.$$

The additional integrals of motion for the cases $\omega_z/\omega_\rho = 1/2$ ($m = 0$) and $\omega_z/\omega_\rho = 2$, Eq. (32), can be treated as the ρ and z-components of a generalized Runge–Lenz vector

$$\mathbf{c} = \mathbf{a} + \mathbf{b}(\rho, z), \quad (B.13)$$

respectively. Here $\mathbf{b}$ is assumed to be dependent on the positions only, whereas the Runge–Lenz vector contains the momenta. This is the essence of the ansatz. In our case the components of vector $\mathbf{b}$ are

$$b_\rho = -\tilde{\omega}_z^2 z^2 \rho, \quad b_\varphi = 0, \quad b_z = -\tilde{\omega}_\rho^2 \rho^2 z. \quad (B.14)$$

Now we construct the additional integral of motion for the case $\omega_z/\omega_\rho = 1/2$ with an arbitrary m from the length of the vector (B.13) in the xy-plane

$$C^2 = c_\rho^2 + c_\varphi^2 + \delta = (a_\rho - \tilde{\omega}_z^2 z^2 \rho)^2 + a_\varphi^2 + \delta. \quad (B.15)$$

Since a_φ consists of the kinetic term only, we expect the same form for c_φ, i.e., we put $b_\varphi = 0$. The last term δ is also assumed to be a function of the positions only and, if Eq. (B.15) is an appropriate form for C^2, this term can be determined from the condition $dC^2/d\tau = 0$, i.e.,

$$\frac{d\delta}{d\tau} = -\frac{d}{d\tau}[(a_\rho - \tilde{\omega}_z^2 z^2 \rho)^2 + a_\varphi^2]. \quad (B.16)$$

Using Eqs. (B.12) and (24) one can show that

$$\frac{d}{d\tau}[(a_\rho - \tilde{\omega}_z^2 z^2 \rho)^2 + a_\varphi^2]$$
$$= -8m^2 \tilde{\omega}_z^2 (\rho p_\rho + z p_z) = -4m^2 \tilde{\omega}_z^2 \frac{dr^2}{d\tau}. \quad (B.17)$$

This immediately gives

$$\delta = 4m^2 \tilde{\omega}_z^2 r^2. \quad (B.18)$$

ACKNOWLEDGMENTS

REFERENCES

1. M. A. Kastner, Phys. Today **46**, 24 (1993).
2. R. C. Ashoori, Nature (London) **379**, 413 (1996).
3. L. Jacak, P. Hawrylak, and A. Wojs, *Quantum Dots* (Springer, Berlin, 1998).
4. L. P. Kouwenhoven, D. G. Austing, and S. Tarucha, Rep. Prog. Phys. **64**, 701 (2001).
5. J. M. Elzerman, R. Hanson, L. H. W. van Beveren, et al., *Lecture Notes in Physics* (Springer, Berlin, 2005), Vol. 667, p. 25.
6. T. Chakraborty, *Quantum Dots: A Survey of the Properties of Artificial Atoms* (North-Holland, Amsterdam, 1999).
7. P. A. Maksym, H. Imamura, G. P. Mallon, and H. Aoki, J. Phys.: Condens. Matter **12**, R299 (2000).
8. A. Bohr and B. R. Mottelson, *Nuclear Structure* (Benjamin, New York, 1975).
9. S. G. Nilsson and I. Ragnarsson, *Shapes and Shells in Nuclear Structure* (Cambridge Univ. Press, Cambridge, 1995).
10. M. Brack, Rev. Mod. Phys. **65**, 677 (1993); W. A. de Heer, Rev. Mod. Phys. **65**, 611 (1993); V. O. Nesterenko, Phys. Part. Nucl. **23**, 1665 (1992).
11. L. P. Kouwenhoven, C. M. Marcus, P. L. McEuen, et al., in *Mesoscopic Electron Transport, Proceedings of the NATO Advanced Study Institute on Mesoscopic Electron Transport*, Ser. E345, Ed. by L. L. Sohn, L. P. Kouwenhoven and G. Schon (Kluwer, Dordrecht, Boston, 1997), p. 105.
12. Ch. Sikorski and U. Merkt, Phys. Rev. Lett. **62**, 2164 (1989).
13. V. Fock, Z. Phys. **47**, 446 (1928); C. G. Darwin, Proc. Cambridge Philos. Soc. **27**, 86 (1930).
14. W. Kohn, Phys. Rev. **123**, 1242 (1961).
15. L. Brey, N. F. Johnson, and B. I. Halperin, Phys. Rev. B **40**, 10 647 (1989).
16. Q. P. Lie, K. Karrai, S. K. Yip, et al., Phys. Rev. B **43**, 5151 (1991).
17. T. Demel, D. Heitmann, P. Grambow, and K. Ploog, Phys. Rev. Lett. **64**, 788 (1990).
18. B. Meurer, D. Heitmann, and K. Ploog, Phys. Rev. B **48**, 11 488 (1993).
19. V. Gudmundsson and R. R. Gerhardts, Phys. Rev. B **43**, 12 098 (1991).
20. D. Phannkuche and R. R. Gerhardts, Phys. Rev. B **44**, 13 132 (1991).
21. M. Dineykhan, S. A. Zhaugasheva, and R. G. Nazmitdinov, Zh. Eksp. Teor. Phys. **119**, 1210 (2001) [JETP **92**, 1049 (2001)].
22. S. Tarucha, D. G. Austing, T. Honda, et al., Phys. Rev. Lett. **77**, 3613 (1996).
23. Y. Nishi, Y. Tokura, J. Gupta, et al., Phys. Rev. B **75**, 121 301R (2007).
24. Y. Nishi, P. A. Maksym, D. G. Austing, et al., Phys. Rev. B **74**, 033306 (2006).
25. M. Macucci, K. Hess, and G. J. Iafrate, Phys. Rev. B **48**, 17 354 (1993); J. App. Phys. **77**, 3267 (1995).
26. W. D. Heiss and R. G. Nazmitdinov, Phys. Lett. A **222**, 309 (1996).
27. A. Wojs, P. Hawrylak, S. Fafard, and L. Jacak, Phys. Rev. B **54**, 5604 (1996).
28. M. Dineykhan and R. G. Nazmitdinov, Phys. Rev. B **55**, 13 707 (1997).
29. M. Stopa, Phys. Rev. B **54**, 13 767 (1996).
30. S. M. Reimann and M. Manninen, Rev. Mod. Phys. **74**, 1283 (2002).
31. Y. Alhassid, Rev. Mod. Phys. **72**, 895 (2000).
32. W. D. Heiss and R. G. Nazmitdinov, Phys. Rev. B **55**, 16 310 (1997).
33. W. D. Heiss and R. G. Nazmitdinov, Pis'ma Zh. Eksp. Teor. Phys. **68**, 870 (1998) [JETP Lett. **68**, 915 (1998)].
34. R. P. Feynman, Phys. Rev. **56**, 340 (1939).

35. H. A. Jahn and E. Teller, Proc. R. Soc. London A **161**, 220 (1937).
36. W. D. Heiss and R. G. Nazmitdinov, Phys. Rev. Lett. **73**, 1235 (1994); Physica D **118**, 134 (1998).
37. S. Tarucha and D. G. Austing, Tokura Y, et al., Phys. Rev. Lett **84**, 2485 (2000).
38. W. D. Heiss, R. G. Nazmitdinov, and S. Radu, Phys. Rev. C **52**, 3032 (1995).
39. R. G. Nazmitdinov, N. S. Simonovic, and J. M. Rost, Phys. Rev. B **65**, 155 307 (2002).
40. N. S. Simonovic and R. G. Nazmitdinov, Phys. Rev. B **67**, 041305R (2003).
41. L. D. Landau and E. M. Lifshitz, *Quantum Mechanics* (Nauka, Moscow, 1974; Pergamon, Oxford, 1977).
42. J. M. Jauch and E. L. Hill, Phys. Rev. **57**, 641 (1940).
43. R. Blümel, C. Kappler, W. Quint, and H. Walther, Phys. Rev. A **40**, 808 (1989).
44. Y. Alhassid, E. A. Hinds, and D. Meschede, Phys. Rev. Lett. **59**, 1545 (1987).
45. I. V. Komarov, L. I. Ponomarev, and S. Yu. Slavyanov, *Spheroidal and Coulomb Spheroidal Functions* (Nauka, Moscow, 1976) [in Russian].
46. P. Hawrylak, Phys. Rev. Lett. **71**, 3347 (1993).
47. R. C. Ashoori, H. L. Stormer, J. S. Weiner, et al., Phys. Rev. Lett. **71**, 613 (1993).
48. T. Schmidt, M. Tewordt, R. H. Blick, et al., Phys. Rev. B **51**, 5570 (1995).
49. L. P. Kouwenhoven, T. H. Oosterkamp, M. W. S. Danoe-sastro, et al., Science **278**, 1788 (1997).
50. J. J. Palacios, L. Martin-Moreno, G. Chiappe, et al., Phys. Rev. B **50**, 5760 (1994).
51. A. H. MacDonald, S.-R. Eric Yang, and M. D. Johnson, Aus. J. Phys. **46**, 345 (1993).
52. M. Wagner, U. Merkt, and A. V. Chaplik, Phys. Rev. B **45**, 1951 (1992); F. M. Peeters and V. A. Schweigert, Phys. Rev. B **53**, 1468 (1996); M. Dineykhan and R. G. Nazmitdinov, J. Phys.: Condens. Matter. **11**, L83 (1999).
53. C. Ellenberger, T. Ihn, C. Yannouleas, et al., Phys. Rev. Lett. **96**, 126 806 (2006).
54. D. V. Melnikov and J-P. Leburton, Phys. Rev. B **73**, 085 320 (2006).
55. R. G. Nazmitdinov and N. S. Simonovic, Phys. Rev. B , 193 306 (2007).
56. P. A. Maksym, Physica B **184**, 385 (1993).
57. Ll. Serra, R. G. Nazmitdinov, and A. Puente, Phys. Rev. B **68**, 035341 (2003).
58. C. Yannouleas and U. Landman, Phys. Rev. Lett. **85**, 1726 (2000).
59. B. Szafran, S. Bednarek, and J. Adamowski, J. Phys.: Condens. Matter **15**, 4189 (2003).
60. C. Creffield, Häusler W., Jefferson J. H., Sakar S., Phys. Rev. B **59**, 10 719 (1999).
61. A. Puente, Ll. Serra, and R. G. Nazmitdinov, Phys. Rev. B **69**, 125 315 (2004).
62. A. J. Lichtenberg and M. A. Liberman, *Regular and Stochastic Motion* (Springer, New York, 1983).
63. I. S. Gradshteyn and I. M. Ryzhik, *Table of Integrals, Series, and Products*, 5th ed. (Academic, New York, 1994), pp. 898, 1096.
64. D. M. Zumbühl, C. M. Marcus, M. P. Hanson, and A. C. Gossard, Phys. Rev. Lett. **93**, 256 801 (2004).